LITHOS 350-351 (2019) 105215

Contents lists available at ScienceDirect

LITHOS

journal homepage: www.elsevier.com/locate/lithos

Geochemistry and mineralogy of serpentinization-driven hyperalkaline springs in the Ronda peridotites

Manolis Giampouras [a], Carlos J. Garrido [a], Jennifer Zwicker [b], Iñaki Vadillo [c], Daniel Smrzka [b], Wolfgang Bach [e, f], Jörn Peckmann [d], Pablo Jiménez [c], José Benavente [g], Juan Manuel García-Ruiz [a, *]

[a] Andalusian Institute of Earth Sciences (IACT), CSIC – UGR, Avenida de Las Palmeras 4, 18100, Armilla, Granada, Spain
[b] Department of Geodynamics and Sedimentology, University of Vienna, A-1090, Vienna, Austria
[c] Center of Hydrogeology, University of Malaga, 29071, Malaga, Spain
[d] Institute for Geology, Department of Earth Sciences, University of Hamburg, 20146, Hamburg, Germany
[e] MARUM-Center of Marine and Environmental Sciences, 28359, Bremen, Germany
[f] Geoscience Department, University of Bremen, 28359, Bremen, Germany
[g] The Water Institute, University of Granada, 18003, Granada, Spain

ARTICLE INFO

Article history:
Received 14 March 2018
Received in revised form
20 September 2019
Accepted 28 September 2019
Available online 16 October 2019

Keywords:
Ronda peridotites
Serpentinization
Alkaline springs
Carbonate precipitation
Magnesium ion effect

ABSTRACT

We present a detailed study of the water geochemistry, mineralogy and textures in serpentinization-related hyperalkaline springs in the Ronda peridotites. Ronda waters can be classified into hyperalkaline fluids and river waters that are broadly similar to Ca^{2+}–OH^- and Mg^{2+}–HCO_3^- water types described in serpentinite-hosted alkaline springs elsewhere. At the discharge sites of the fluids (fractures or human made outlets) and ponds along the fluid flow paths, the fluids are hyperalkaline ($10.9 < pH < 12$) and characterized by low Mg and high Na, K, Ca, and Cl^- concentrations. River waters, occurring near the spring sites, are mildly alkaline ($8.5 < pH < 8.9$) and enriched in Mg and DIC compared to Na, K, Ca and Cl^-. The chemistry of Ronda Mg–HCO_3 river waters is likely due to the hydrolysis of ferromagnesian peridotite minerals in equilibrium with the atmosphere by infiltrated meteoric water and shallow groundwater in the serpentinized peridotite. The Ronda Ca–OH hyperalkaline fluids are generated by the combination of low temperature serpentinization reactions from infiltrated surface Mg–HCO_3 river waters —or Ca–HCO_3 waters from near karst aquifers— and deep carbonate precipitation isolated from atmospheric CO_2. Mass balance calculations indicate that the weathering of Ca-bearing peridotite silicates, such as diopside, is a feasible source of Ca in Ronda Ca–OH hyperalkaline fluids; however, it requires steady-state dissolution rates substantially greater than those determined experimentally.

Travertine, crystalline crusts and sediment deposits comprise the types of solid precipitates observed in Ronda hyperalkaline spring sites. Calcite, aragonite, dolomite and Mg-Al-rich clays are the main mineral phases identified in the spring sites. As illustrated in the Baños del Puerto spring site, (i) calcite-dominated precipitation is due to uptake of atmospheric CO_2 by Ca–OH hyperalkaline fluids during discharge, and (ii) aragonite-dominated precipitation is due to mixing of Ca–OH hyperalkaline fluids with Mg–HCO_3 river waters. Aragonite and dolomite contents increase away from the springs and toward the river waters that uniquely reflects the effect of Mg ions on the precipitation of aragonite versus calcite. Other potential factors controlling the precipitation of these $CaCO_3$ polymorphs are the Mg/Ca ratio, the CO_2 content, and the temperature of the fluids. Dolomite forms during lithification of travertine due to periodic flooding of river water combined with subsequent evaporation.

1. Introduction

Carbonation processes associated with hyperalkaline fluids and serpentinization of peridotite have recently attracted much attention because of their relevance to carbon capture and storage (Kelemen et al., 2011; Klein and Garrido, 2011; Matter and Kelemen,

* Corresponding author.
E-mail addresses: juanma.garciaruiz@gmail.com, juanmanuel.garcia@csic.es (J.M. García-Ruiz).

https://doi.org/10.1016/j.lithos.2019.105215

2009), the role of carbonation of serpentinite in the deep carbon cycle (Alt et al., 2012, 2013; Dasgupta and Hirschmann, 2010; Kelemen and Manning, 2015; Menzel et al., 2018, 2019), the origin of prebiotic organic chemistry (Martin et al., 2008; Martin and Russell, 2007; Sleep et al., 2011), and the detection of primitive life (Garcia-Ruiz et al., 2003, 2017).

Active serpentinization in the ocean sub-seafloor generates fluid vents with carbonate chimneys —up to 60 m in height— composed of mixtures of calcite, aragonite, and brucite (Ludwig et al., 2006). The Lost City hydrothermal field is a unique example of active serpentinization system in the Atlantis massif oceanic core complex near the Mid-Atlantic Ridge at 30º N (Kelley et al., 2001). In this vent field, the discharging alkaline to hyperalkaline fluids (pH, 9–11) show relatively low temperature (40–90 °C), high H_2/CH_4 ratios, and low concentrations of metals (Kelley et al., 2005; Proskurowski et al., 2006). Alkaline to hyperalkaline springs also occur off-shore in continental settings, where hyperalkaline fluids form during deep circulation of meteoric waters in tectonically emplaced and variably serpentinized ophiolites and subcontinental lithosphere mantle peridotites. In these continental peridotites, the exposure of serpentinite-hosted hyperalkaline (pH > 11) fluids to atmospheric conditions induces carbon mineralization (Neal and Stanger, 1984). Carbonate precipitation in continental serpentinite-hosted hyperalkaline fluids are documented, among other places, in the Samail Ophiolite (Oman) (Chavagnac et al., 2013a; Neal and Stanger, 1983; Paukert et al., 2012), California Coast Range (USA) (Barnes and O'Neil, 1971; Blank et al., 2009; Morrill et al., 2013), Bay of Islands (Canada) (Cardace et al., 2009), Santa Elena Ophiolite (Costa Rica) (Sánchez-Murillo et al., 2014) and the Ligurian ophiolites (Italy) (Chavagnac et al., 2013a; Cipolli et al., 2004). In addition, alkaline springs in Prony Bay ophiolites (New Caledonia) are an example of carbonate precipitation by meteoric-origin hyperalkaline fluids that are subsequently affected by seawater (Monnin et al., 2014). The increasing interest in carbon mineralization for the removal of carbon dioxide from the atmosphere has fueled research on carbonate formation in serpentinite-hosted alkaline fluids in continental settings such as caverns, hot springs, and lacustrine environments (Lacelle et al., 2009; Leleu et al., 2016; Pentecost, 2005).

In the Ronda peridotites (Betic Cordillera, S. Spain) (Fig. 1), previous studies have documented more than 70 alkaline to hyperalkaline springs, which chemistry and related mineralization are still barely known (Etiope et al., 2016; Vadillo et al., 2016). Here, we present a detailed study of the geochemistry of hyperalkaline fluids and river waters, and the associated mineral phases and textures characterizing the alkaline spring sites in the Ronda peridotites. The present study is aimed at better constraining the carbonation processes in serpentinite-hosted alkaline fluids in one of the largest exposures of subcontinental mantle peridotites worldwide.

2. The Ronda peridotites

The Gibraltar arc in the westernmost Mediterranean is bounded by the Alpine Betic and Rif orogenic belt that surrounds the Neogene Alborán Sea basin (Fig. 1a). This arc-like mountain belt was formed as the result of a complex Cenozoic evolution of subduction initiation, slab fragmentation, and rollback in the central and western Mediterranean in a context of slow convergence between Africa and Europe (e.g., Balanyá et al., 1997; Booth-Rea et al., 2015; Faccenna et al., 2004; Guerrera et al., 2005; Lonergan and White, 1997; Platt et al., 2013; Royden, 1993). These geodynamic processes resulted in the crustal emplacement of large bodies of subcontinental mantle peridotites that now crop out in the internal zones of the western Betics (the Ronda peridotites) and the Rif (Beni Bousera peridotites) mountain belts (Fig. 1a) (Frets et al., 2014; Garrido et al., 2011; Hidas et al., 2013a; Marchesi et al., 2012; Mazzoli et al., 2013; Obata et al., 1980; Précigout et al., 2013; Tubía et al., 1997; Van der Wal and Vissers, 1996).

In the Betic Cordillera, several mantle peridotite massifs —here collectively referred to as "the Ronda peridotites"— occur in the westernmost Alpujárride complex, a tectonic unit of the internal zones of the Betics that is structurally sandwiched between the Maláguide and the Nevado-Filábride complexes (Fig. 1a). The westernmost Alpujárride complex includes the Jubrique and Blanca crustal units that overlie and underlie, respectively, the Ronda peridotite massif (Fig. 1 a & b) (Balanyá et al., 1997; Tubía et al., 1997). The Jubrique unit is a highly attenuated (≤ 5 km) crustal section composed of non-metamorphic to greenschist carbonates underlain by a crustal sequence of increasing metamorphic grade towards the upper contact with the peridotite massif. The Blanca Unit (Fig. 1b) underlies below the Ronda peridotite and is composed of variably deformed, high temperature–low pressure schists, marbles, and migmatitic gneisses (Acosta-Vigil et al., 2014; Tubía et al., 1997).

Covering an area of c. 450 km^2, the Ronda peridotites are one of the largest outcrops of subcontinental mantle peridotite worldwide (Obata et al., 1980; Tubía et al., 1997). These ultramafic massifs are mostly composed of spinel and plagioclase peridotite (lherzolite, minor harzburgite and subordinate dunite) and minor garnet lherzolite, with occasional layers of garnet- spinel- and plagioclase-pyroxenites, and rare gabbro veins and chromitite pods (Bodinier et al., 2008; Garrido and Bodinier, 1999; Garrido et al., 2011; Gervilla and Leblanc, 1990; González-Jiménez et al., 2017; Lenoir et al., 2001; Obata et al., 1980; Soustelle et al., 2009; Tubia et al., 2004; Van der Wal and Vissers, 1996). The Ronda peridotites encompass several massifs exposed in the mountain ranges of Sierra Bermeja (Ronda massif), Sierra Alpujata (Ojén massif), and Sierra de Aguas (Carratraca massif) (Fig. 1b). The massifs are in tectonic contact with different crustal lithologies of the Jubrique and the Blanca units of the western Alpujarrides, and the frontal units of the western internal zones of the Betics (Martín Algarra, 1987) (Fig. 1b).

3. Hyperalkaline springs in the Ronda peridotites

We studied five hyperalkaline spring sites in the westernmost part of the Ronda peridotites (Fig. 1b; Table 1). Etiope et al. (2016) investigated the stable isotope signatures and ^{14}C age of gases occurring in these spring sites and confirmed that they show isotopic signatures similar to other continental hyperalkaline springs associated with active serpentinization. The spring sites investigated in the present study generally occur near the contact of peridotites with crustal rocks (Fig. 1b). Fuente Amargosa (AMAR), Fuente Alfaguara (ALF) and Balneario de Tolox (BAL) springs are located in the eastern part of Sierra Bermeja —the Ronda peridotite massif— near the village of Tolox (Fig. 1b), and the La Hedionda (HED) spring is located in SE Sierra de Aguas —Carratraca peridotite massif— near the village of Álora (Fig. 1b). In these springs, the hyperalkaline fluids emanate from rock fractures (ALF) or human-made pipes and fountains (BAL, AMAR, and HED).

The Baños del Puerto (BP) (Fig. 2) —in the Ojén massif, SW Sierra Alpujata (Fig. 1b)— is a serpentinite-hosted spring system near the riverside of the Alaminos river. We selected this spring site for the comprehensive investigation of hyperalkaline fluids and river waters, and the associated mineralogy. Fig. 2a shows a map of the BP spring system; the hyperalkaline fluids emanate from fractures in serpentinized peridotites (e.g., BP1, BP3, and BP5; Fig. 2a and b) and flow downstream stagnating at shallow ponds along several flow paths (e.g., BP1/SK and BP2; Fig. 2a and c). The hyperalkaline fluids discharge at the riverside, where they mix with the Alaminos river waters (Fig. 2 a & d). Rarely, small and isolated shallow reddish

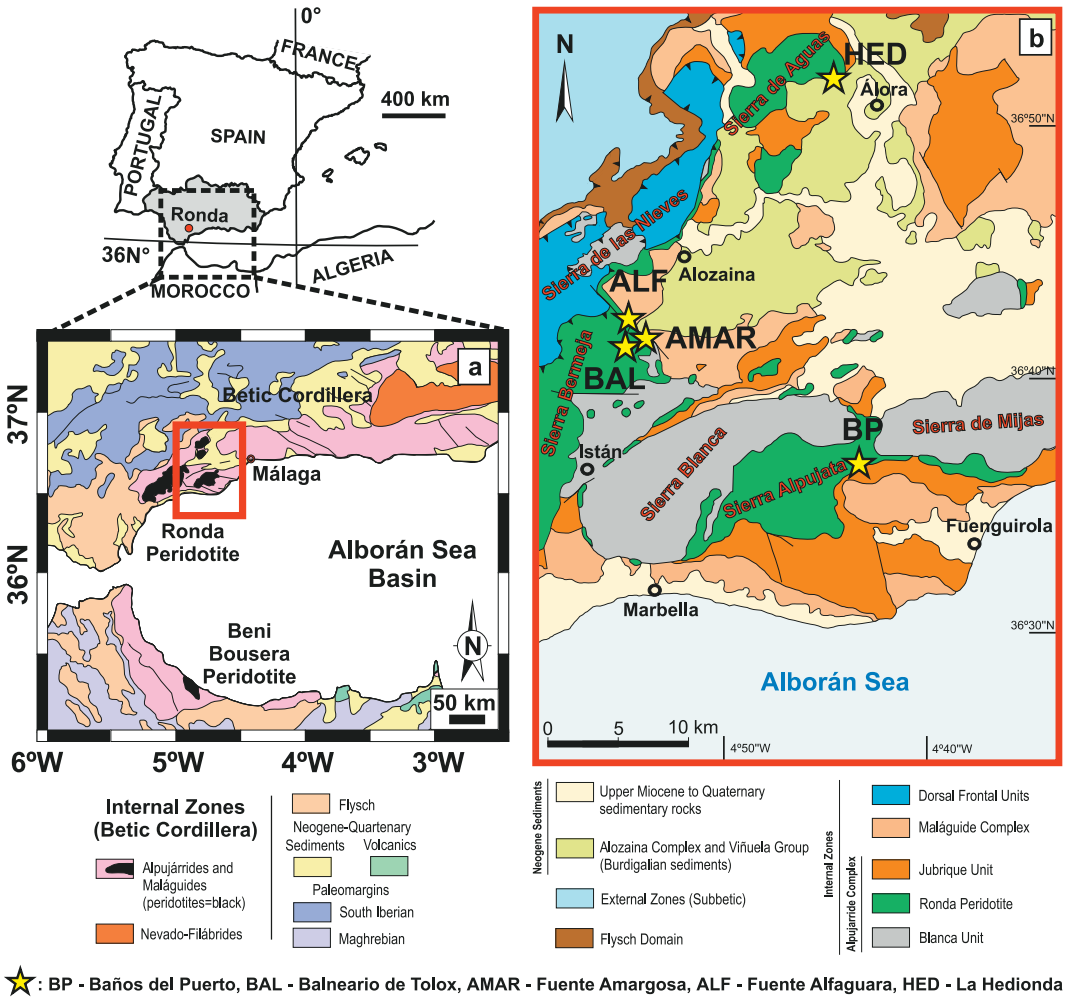

Fig. 1. Geological maps of the Betic-Rif orogen and the western Betic Cordillera. **a)** Simplified geological map of the main tectonic domains and units of the Betic-Rif orogenic belt showing the location of the Ronda peridotites (Betic Cordillera, S. Spain) and the Beni Bousera Peridotite (Rif Belt, N. Morocco). The red rectangle indicates the area shown in Fig. 1b (modified after Hidas et al., 2013a). **b)** Enlarged geological map of the western sector of the internal zones of the Betic Cordillera showing the location of the investigated serpentinite-hosted hyperalkaline spring sites (yellow stars) in eastern Sierra Bermeja (Ronda peridotite massif: BAL: Balneario de Tolox; AMAR: Fuente Amargosa; ALF: Fuente Alfaguara), western Sierra Alpujata (Ojén peridotite massif: BP: Baños del Puerto), and northwestern Sierra de Aguas (Carratraca peridotite massif: HED: La Hedionda) (modified after Acosta-Vigil et al., 2014; Mazzoli and Martin Algarra, 2011). (For interpretation of the references to color in this figure legend, the reader is referred to the Web version of this article.)

ponds occasionally occur in this spring site (e.g., BP5; Fig. 2a and e). Intermittent methane bubbling (Etiope et al., 2016) is observed in some ponds (e.g., BP2 and BP5; Fig. 2a) and in the river at the confluence with the hyperalkaline streams.

In Ronda hyperalkaline spring sites, the main types of precipitates are travertines, crystalline crusts and sediments (Fig. 2c

Table 1
General sample information and water chemistry parameters.

Sample ID	Peridotite Massif	Coordinates		pH	T	Cond.	Alk.
		N	W		(°C)	(μS/cm)	(meq/L)
Hyperalkaline fluids							
HED	Carratraca	36°50′34.55″	4°43′57.72″	11.3	21.0	857	2.32
AMAR	Ronda	36°41′21.24″	4°54′39.92″	11.8	18.2	1257	5.08
BAL	Ronda	36°40′44.44″	4°54′34.34″	11.4	16.9	478	1.54
ALF	Ronda	36°41′35.12″	4°55′00.56″	12.0	18.9	1100	6.02
BP1	Ojén	36°35′42.18″	4°43′32.11″	11.5	21.6	636	2.33
BP1/SK	Ojén	36°35′42.11″	4°43′32.26″	11.5	20.1	586	1.21
BP2	Ojén	36°35′41.76″	4°43′32.12″	11.5	20.2	718	2.73
BP3	Ojén	36°35′42.12″	4°43′32.33″	10.9	20.1	1859	1.79
BP4	Ojén	36°35′42.32″	4°43′32.42″	11.4	20.3	1156	2.47
BP5	Ojén	36°35′42.41″	4°43′32.54″	9.6	20.8	3015	15.13
River waters							
ALF/R	Ronda	36°41′34.98″	4°55′01.51″	8.8	16.8	412	5.26
BPR/DO	Ojén	36°35′41.84″	4°43′32.38″	8.9	17.7	621	8.32
BPR/UP	Ojén	36°35′43.10″	4°43′33.02″	8.5	17.6	550	8.37

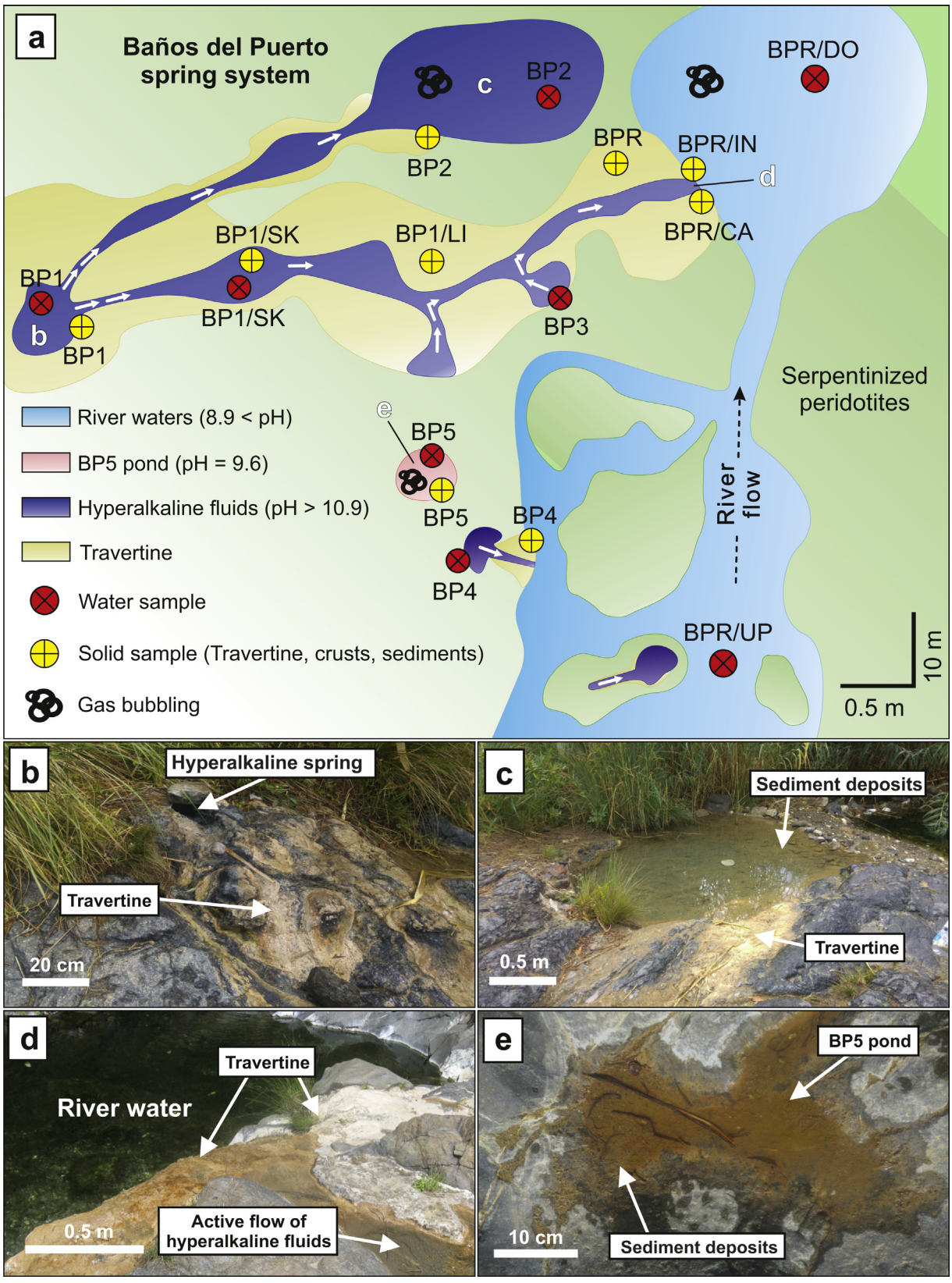

Fig. 2. Overview of Baños del Puerto site (BP). **a)** Sketch of the serpentinite-hosted BP hyperalkaline spring system in Sierra Alpujata (Fig. 1b) near Alaminos river. The BP site hosts numerous springs of hyperalkaline fluids discharging from fractures in the serpentinized peridotites. The hyperalkaline fluids flow (white arrows) towards the riverside, locally stagnating in shallow ponds, and eventually mixing with the Alaminos river waters. Also shown are travertine zones on bedrock, sampling locations of solid (yellow circles) and water (red circles) samples, and sites with gas bubbling. The IDs of water (e.g. BP1) and solid (e.g. BP1/SK) samples in the figure correspond to the IDs presented in Tables 1 and 2 for the water samples and in Table 3 for the solid samples. **b)** Picture of travertine forming around the hyperalkaline spring (BP1; label b in Fig. 2a). **c)** Picture of spring-pond systems of hyperalkaline fluids (BP2; label c in Fig. 2a) with travertine and sediment deposits, and periodic gas bubbling. **d)** Picture of the confluence and mixing site of hyperalkaline fluids and river waters (label d in Fig. 2a). Note the presence of travertine on the bedrock along the flow path of hyperalkaline fluids and the development of thick travertine at the mixing zone with river waters. **e)** Picture of the red-colored isolated pond, BP5, showing the sediment bed at the bottom of the pond (label e in Fig. 2a). (For interpretation of the references to color in this figure legend, the reader is referred to the Web version of this article.)

and e). Crystalline crusts occur as thin films floating on the surface of hyperalkaline ponds, while sediments —referred to as "flocs" in the Oman alkaline springs (e.g., Falk et al., 2016)— are unconsolidated solid precipitates on the bottom of the ponds. Pentecost (2005) defines travertine as the inorganic process of calcium carbonate precipitation through the transfer (evasion or invasion) of carbon dioxide from or to a groundwater source. In this study, we refer to travertine as the solid precipitates at the spring discharging sites, and to lithified terraces in former and current flow paths of hyperalkaline fluids (Fig. 2b–d). All the studied hyperalkaline spring sites are characterized by different extents of travertine precipitation and build-up of lithified terraces.

The HED and AMAR sites (Fig. 1b) show only minor amounts of travertine, and the BAL site contains only sediments. The ALF site hosts travertine precipitating around the discharge site of the hyperalkaline spring, and crystalline crusts forming on the surface of the discharging fluids. The BP site has abundant travertine, crystalline crusts, and sediments depositing in various ponds. No evident precipitation was observed at the riverbeds (Fig. 2a).

4. Sampling

We sampled water and —where present— solid samples of mineralization from the hyperalkaline spring sites, some of which also accommodate river waters (i.e. ALF and BP sites). Solid samples were taken from travertines, crystalline crusts, and sediments (cf. Section 3). Where available, we collected travertine samples at the spring discharging sites, along the flow paths, and from lithified terraces.

We collected water samples from the discharging sites (e.g., BP1 spring in Fig. 2b) and ponds (e.g., BP2 pond in Fig. 2c) of hyperalkaline fluids, and at selected sites, from nearby river waters (e.g., Fig. 2d). We sampled hyperalkaline waters from the discharging sites of the BAL, AMAR, ALF, and HED springs (Table 1), and one sample of the river waters in the ALF site (Table 1). In the BP site, we sampled hyperalkaline fluids from discharging sites and ponds, river waters, and waters from an isolated, red-colored pond (Fig. 2a). The locations of these samles are given in Table 1.

Water samples were taken using 50 mL syringes (PE/PP) with cellulose acetate membrane filters (Sartorius Minisart Plus; pore diameter 0.45 μm) that were previously rinsed with the sampled water. The water samples were split into three 10 mL polyethylene vials —cleaned with milliQ water— for the measurement of alkalinity, cations and trace metals, and anions, respectively. The vials for the determination of alkalinity were filled without headspace, while the vials for cation and trace metal analyses were preconditioned with 5% HNO_3 (distilled), and 100 μL of concentrated HNO_3 (distilled) were added to the water samples.

5. Methodology

5.1. In situ measurements of physicochemical parameters of waters

We determined in situ the pH (±0.01), temperature (±0.4 °C), total dissolved solids (±1%) and electrical conductivity (±1%) of water samples using a Hanna Instruments HI 9813–5 portable meter. We measured the alkalinity within 1 h after sampling by pouring 10 mL of the water sample into a 20 mL polystyrene container on a portable magnetic stirrer; after measurement, 0.1 M HCl (Titrisol, Merck, Germany) was added in 20 μL steps under continuous stirring until attaining a pH value between 3.5 and 4.3. The alkalinity (*Alk.*) is calculated as:

$$Alk.\left(\frac{mol}{L}\right)=\frac{\left[(VHCl\cdot cHCl)-10^{-pHfinal}\cdot\frac{(V0+VHCl)}{fH+}+10^{-pHstart}\cdot\frac{V0}{fH+}\right]}{V_0} \quad [1]$$

where V_0 is the initial sample volume, V_{HCl} and C_{HCl} are, respectively, the volume and the concentration of the acid added, pH_{start} and pH_{final} are, respectively, the pH at the start and end of the titration, and f_{H+} is the activity coefficient of H^+ ions (1.0 for freshwater). A 2.5 M of $NaHCO_3$ solution was measured as a control in order to determine the accuracy and the precision of the method. Precision was better than 0.6% and accuracy was < 3.4%.

Dissolved Inorganic Carbon (DIC) was calculated using the alkalimetric titration equation of Stumm and Morgan (1996):

$$C_T\left(\frac{mmol}{L}\right)=1000\cdot\frac{\left(\frac{Alk}{1000}+[H^+]-[OH^-]\right)}{(\alpha_1+2\alpha_2)} \quad [2]$$

where C_T is the sum of the concentrations of carbonic species in the aqueous solution, and α_1 and α_2 are the values of ionization fractions of carbonic acid. Ionization fractions were estimated using the equilibrium constants, $K_1=[H^+][HCO_3^-]/[H_2CO_3]$ for HCO_3^-, and $K_2=[H^+][CO_3^{2-}]/[HCO_3^-]$ for CO_3^{2-}.

5.2. Analyses of solid and water samples

The mineralogy of solid samples was determined by powder X-ray diffraction (XRD), using a PANalytical MPD diffractometer with a Bragg-Brentano parafocusing geometry and Cu K_a radiation (operating at 40 mA and 45 kV) at the Andalusian Institute of Earth Sciences (IACT, Granada, Spain). Instrument configuration included programmable divergence slits in the incident and diffracted beams, placement of a 0.25° fix anti-scatter slit in the incident path and a PSD detector PIXel. Data processing was conducted using the software HighScore Plus from PANalytical X'Pert PRO (mineral database: Pdf2HSP/PAN-ICSD). Mineral quantification was defined by peak refining method described in Rietveld (1969). The observation and semi-quantitative analysis of solid samples was carried out at the Centro de Instrumentación Científica (CIC) of the University of Granada (Granada, Spain) using a Field Emission ZEISS AURIGA (InLens mode at 3 kV) and a Variable Pressure SEM FEI QEMSCAN 650F (SE mode at 5 kV and BSE mode at 12 kV) Scanning Electron Microscope (SEM), both equipped with Energy Dispersive X-ray Spectrometers (EDS).

Water samples were analyzed for major (Ca, K, Mg, Na, Si, P) and trace elements (Ba, Sr, Al, Fe) by inductively coupled plasma optical emission (ICP-OES) spectroscopy using a Varian Vista Pro ICP-OES at the University of Bremen. The analyses were conducted within two weeks after sampling. Sulfate (SO_4^{2-}) and chloride (Cl^-) concentrations were determined using a Metrohm 882 Compact IC Plus ion chromatograph (IC) at the University of Bremen. The relative error (%) for SO_4^{2-} and Cl^- is 1.9% and 1.4%, respectively, and it was obtained from the measurement of certified reference material (CRM) TMDW-A/IAPSO (seawater). The percentage errors for the ICP-OES measurements were obtained by using the SLEW-3/evisa (estuarine water) and SLRS-5/evisa (river water) CRMs and they are < 5% for Ca, Ba, Mg, Na, Si, Sr, Al and Fe, 10% for K, and 24% for P.

5.3. PHREEQC modelling

The Saturation Index (SI) of the relevant mineral phases in the sampled waters was calculated using the PHREEQC-2 code (Parkhurst and Appelo, 2005) and the wateq4f.dat database (Ball and Nordstrom, 1991). Negative SI indicates that the solutions are

undersaturated with respect to a given mineral and its dissolution is thermodynamically favored over precipitation; positive SI indicates that mineral precipitation is favored, and SI of zero shows that the mineral phase is in equilibrium with the solution. We removed serpentine-group minerals, diopside, talc, and other minerals from the dataset that, though could be supersaturated (SI > 5) in the investigated alkaline fluids, do not precipitate in alkaline terrestrial systems (Paukert et al., 2012; Chavagnac et al., 2013b).

We use PHREEQC-2 to model the chemical variations of the waters induced by a gradual CO_2 partial pressure (pCO_2) decrease (cf. Section 6.1) to simulate non-reactive isolation of the waters from the atmosphere. The step of pCO_2 decrease was −0.25 bar, and the final pCO_2 of the waters was −9.17 bar. The model used Ronda river waters (sample BPR/DO in Table 2) and Ca–HCO_3-rich waters from the Turón river valley in eastern Serranía de Ronda (Barberá and Andreo, 2015).

6. Results

6.1. Classification of Ronda alkaline and hyperalkaline waters

Based on their chemistry and physical characteristics, we classify Ronda waters into hyperalkaline fluids and river waters (Figs. 3 and 4):

i. Hyperalkaline fluids are characterized by high pH (10.9 − 12) (Table 1), low Mg (0.0007 to ~0.06 mmoL/L) and high Na (up to ~4.6 mmoL/L), K (up to ~0.34 mmoL/L), Ca (up to ~1.9 mmoL/L), and Cl^- (up to ~4.5 mmoL/L) concentrations compared to those of river waters (Fig. 3a and b). Hyperalkaline fluids display relatively constant DIC/Ca ratios and fall close to the Ca apex in the Ca − DIC − Si diagram (Fig. 3d). On the contrary, these fluids show variable DIC/Mg ratios plotting along the DIC − Si side (Fig. 3e). They correspond to water samples taken from discharge sites —from natural or human-made outlets, and fractures— and ponds formed along the flow path of the hyperalkaline discharging sites (i.e., in the BP site; Fig. 2b, d & e).

ii. River waters are samples taken from rivers at the ALF and BP sites (Fig. 1). They are enriched in Mg (up to ~2.8 mmoL/L) and DIC (up to ~8.3 mmoL/L) compared to Na, K, Ca and Cl^- (Fig. 3a and b), are mildly alkaline (8.5 < pH < 8.9) (Table 1), and have high alkalinity (Fig. 3b and c). They fall near the DIC − Si side in the Ca − DIC − Si ternary plot (Fig. 3d) and have DIC/Mg ratios between 3 and 4 (Fig. 3).

The BP5 —a red-colored pond (Fig. 2c)— water sample is unlike other alkaline water sample from our study and is characterized by relatively high temperature in the high-end range of hyperalkaline fluids (20.8 °C), and intermediate pH (9.6) between those of river waters and hyperalkaline fluids (Fig. 4a). It shows the highest conductivity (3015 μS/cm) and alkalinity (15.13 meq/L) (Fig. 4b and c) and demonstrates low Ca concentration compared to Mg, Na and K (Fig. 3a). Furthermore, the BP5 falls near the DIC apex in the Ca − DIC − Si diagram (Fig. 3d) and near the Mg apex in the Mg − DIC − Si diagram (Fig. 3e).

Overall, the chemistry of Ronda alkaline waters is within the range of Ca–OH (i.e., Ca^{2+}–OH^--rich) and Mg–HCO_3 (i.e., Mg^{2+}–HCO_3^--rich) water types described in ophiolite-hosted alkaline springs (e.g., Barnes et al., 1967; Barnes and O'Neil, 1969) (Figs. 3 and 4). The composition of Ronda hyperalkaline fluids and river waters are similar to that of hyperalkaline springs and run-off or surface waters —river and shallow groundwater— in the Oman Ophiolite (Fig. 3a–c). Ronda river waters have higher Mg and DIC than Oman surface waters.

Ronda hyperalkaline fluids have a higher conductivity (avg. of 892 μS/cm) and are hotter (avg. of 19.9 °C) (Fig. 4a and b) and less alkaline (avg. 2.68 meq/L) (Fig. 4c) than Ronda river waters (avg. of 17.2 °C, 528 μS/cm and 7.31 meq/L, respectively). Compared to other alkaline spring sites worldwide, Ronda river waters (5 − 8.5 meq/L; Fig. 4c) display a similar range of alkalinity to the Troodos Mg–HCO_3 waters (4.5–9.4 meq/L; Neal and Shand, 2002), and a more restricted range of alkalinity than the Taro-Ceno Valleys Mg–HCO_3 waters (1 − 10.2 meq/L; Boschetti and Toscani, 2008). The Oman Ophiolite Mg–HCO_3-rich, mildly alkaline waters are less alkaline (2.5 − 4.5 meq/L; Chavagnac et al., 2013b) than Ronda river waters (Fig. 4c). The alkalinity of hyperalkaline fluids in the Troodos (2.3 − 6 meq/L; Neal and Shand, 2002), Gruppo di Voltri ophiolites (0.5 − 4.4 meq/L; Cipolli et al., 2004), and Samail Ophiolite (Chavagnac et al., 2013b) are similar to those in the Ronda peridotites (1.2 − 6 meq/L; Fig. 4c).

Temperature and pH of waters from our study —measured in October 2017—are similar (within 0.6 − 1.7 °C, and < 1 for pH) to those measured by Etiope et al. (2016) in the same springs in March and June 2014, pointing to a limited annual and seasonal variability of temperature and pH of Ronda peridotite waters. The temperature of ultramafic-hosted fluids in continental springs, such as in Ronda , are generally lower than those of alkaline fluids in submarine vents like the Lost City hydrothermal field (40 − 90 °C) (Kelley et al., 2001) (Fig. 5). Other continental serpentinite-hosted hyperalkaline fluid sites show similarly low temperatures (Fig. 5); the New Caledonia and Cyprus alkaline springs display temperatures in the

Table 2
Major ion and trace element chemistry of water samples.

Sample ID	Ba (μmol/L)	Ca (mmol/L)	K (mmol/L)	Mg (mmol/L)	Na (mmol/L)	Si (mmol/L)	Al (μmol/L)	Fe (μmol/L)	Sr (μmol/L)	Cl^- (mmol/L)	SO_4^{2-} (mmol/L)	P (μmol/L)	DIC (mmol/L)
Hyperalkaline fluids													
HED	0.3058	0.6545	0.3379	0.0023	4.5846	0.2280	26.683	0.0895	2.0315	4.4939	0.0152	0.4197	0.4117
AMAR	0.0728	1.7406	0.2401	0.0165	3.1766	0.0828	0.7783	0.1612	5.9690	2.0905	0.0375	0.1614	0.4194
BAL	0.0073	0.1437	0.1898	0.0273	1.8930	0.0192	0.8894	0.0358	0.3766	1.5183	0.0015	b.d.l.	0.8219
ALF	0.0146	1.9100	0.2348	0.0007	1.9943	0.0430	5.3738	0.0179	4.1885	1.4955	0.0015	b.d.l.	0.5728
BP1	0.0218	0.8798	0.1364	0.0007	1.9769	0.0851	3.4466	0.0537	2.1228	1.9592	0.0004	0.0323	0.3738
BP1/SK	0.0291	0.2914	0.1822	0.0027	2.5550	0.0990	2.5201	b.d.l.[a]	1.8147	2.5428	0.0055	0.2260	0.5646
BP2	0.0218	0.8835	0.1708	0.0616	2.4332	0.0863	4.4472	0.0537	2.2598	2.3149	0.0007	0.1614	0.4570
BP3	0.0291	0.5761	0.2445	0.0455	3.8560	0.1033	3.5578	0.1433	2.2483	3.9690	0.0245	3.0994	0.8818
BP4	0.0218	0.8276	0.1761	0.0007	2.4628	0.0907	4.2249	0.0179	2.1685	2.4925	0.0008	b.d.l.	0.4504
BP5	0.0874	0.8982	1.1556	9.7305	20.4132	0.0572	1.0377	0.1433	2.4880	29.6431	6.8268	24.569	14.8356
River waters													
ALF/R	0.0146	0.0895	0.0117	1.9885	0.1746	0.3792	0.9636	0.0179	0.1484	0.1677	0.0313	0.0323	5.2287
BPR/DO	0.0874	0.6138	0.0149	2.8031	0.3075	0.6961	0.4818	0.1791	1.6320	0.3152	0.2325	0.2583	8.2862
BPR/UP	0.0437	0.6178	0.0132	2.8216	0.3059	0.7025	0.6300	0.0537	1.6435	0.3108	0.2339	0.3874	8.2797

[a] Below detection limit.

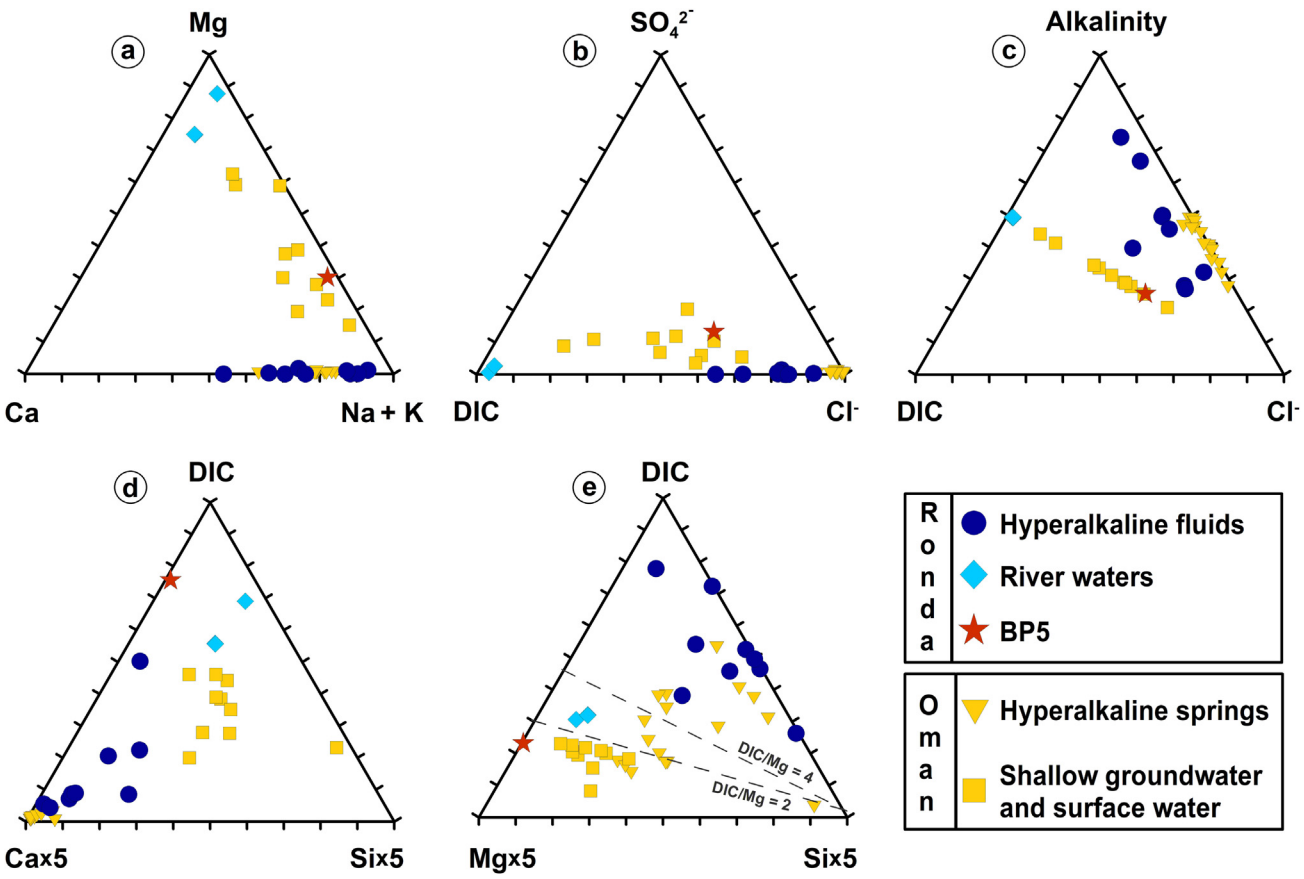

Fig. 3. Ternary classification diagrams of Ronda collected waters (this study) and waters from Samail ophiolites in Oman (Paukert et al., 2012). **a)** Mg-Ca-Na + K, **b)** SO_4^{2-}-DIC-Cl^-, **c)** Alkalinity-DIC-Cl^-, **d)** Ca-DIC-Si and **e)** Mg-DIC-Si.

range of 10 – 30 °C (Barnes et al., 1978; Monnin et al., 2014; Neal and Shand, 2002), and those in the Taro-Ceno valleys are c. 13 °C (Boschetti and Toscani, 2008). The temperature of Ronda alkaline waters is similar to those of serpentinite-hosted alkaline fluids of the Cabeço de Vide (avg. of 19.5 °C) (Marques et al., 2008) and Liguria ophiolites (Chavagnac et al., 2013b).

6.2. The chemical composition of Ronda peridotite waters

Ronda water samples altogether show a positive correlation between Na and Cl^- (Fig. 6). Similar correlations have been reported in other serpentinite-hosted spring sites and ascribed to variable extents of evaporation or mixing with surface freshwater or seawater (Chavagnac et al., 2013a; Monnin et al., 2014). The pH gap observed between Ronda hyperalkaline fluids (pH > 10.9) and river waters (pH < 8.9) (Fig. 4) points to limited mixing of both water types at the time of sampling. Therefore, the Na – Cl^- correlation in Ronda water most likely reflects differences in the salinity of waters due to variable extents of evaporation. The effect of evaporation is particularly significant for the hyperalkaline fluid and BP5 samples. Hyperalkaline fluids in discharging sites and ponds —with intermediate Na and Cl^- concentrations— record moderate to great extent of evaporation; the fluids in the BP5 pond underwent the highest evaporation as attested by their unusually high Cl^- and Na concentrations (Fig. 6).

The chemistry of Ronda waters is shown in Fig. 7. The Ca concentration versus pH is rather scattered (Fig. 7a). The Mg, Si, SO_4^{2-} and DIC concentrations show a decrease from river water towards hyperalkaline fluid composition, while Na concentration displays the opposite trend (Fig. 7b–f). Hyperalkaline fluids are enriched in Ca (up to ~1.9 mmoL/L) and depleted in Mg (avg. of 0.06 mmoL/L) and DIC (avg. of 0.63 mmoL/L). River waters contain higher Mg (up to ~2.8 mmoL/L), Si (up to ~0.7 mmoL/L) and DIC (up to ~8.3 mmoL/L) concentration than hyperalkaline fluids. Compared to river waters, hyperalkaline fluids show higher Na, K, Al, and Cl^- concentrations, while Fe, Ba, Sr, and SO_4^{2-} concentrations are similar in both water types. Fluid from the BP5 pond has an unusual chemical composition characterized by very high Mg, Na, K, Cl^-, and DIC, as well as 1 to 4 orders of magnitude higher P and SO_4^{2-} concentrations than the other Ronda water types (Table 2). Generally, Mg, Si, SO_4^{2-} and DIC concentrations of river waters and hyperalkaline fluids display opposite trends with pH (Fig. 7).

Fig. 8 displays the composition of Ronda water normalized to Cl^- to better depict the primary chemical variations of waters that undergo variable extends of evaporation upon fluid discharge (Chavagnac et al., 2013b; Monnin et al., 2014). The Ca/Cl^- and Na/Cl^- ratios versus pH of Ronda hyperalkaline fluids (Fig. 8a and d) display positive covariations that are more patent than in the non-normalized plots (cf. Fig. 7a and d). Otherwise, the plots of Cl-normalized elemental variations are less scattered but display similar trends for Mg, Si, SO_4^{2-}, and DIC versus pH than the non-normalized concentrations, demonstrating that evaporation has not greatly obliterated the primary compositional trends of the Ronda hyperalkaline fluids and river waters.

6.3. Saturation indices of minerals and pCO_2 of waters

The saturation index (SI) for different minerals in the studied Ronda waters are shown in Fig. 9. Calcite and aragonite are saturated in hyperalkaline fluids and river waters, showing a higher

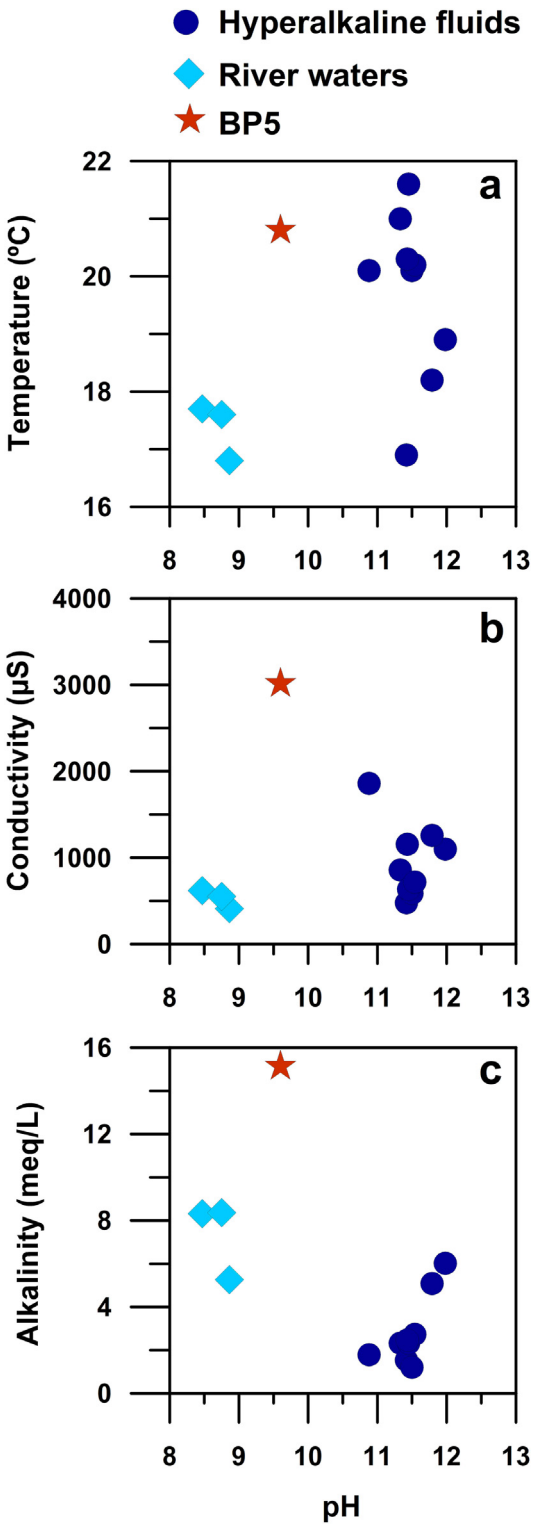

Fig. 4. Water parameters of the collected samples. **a)** temperature, **b)** conductivity, and **c)** alkalinity of water samples versus pH.

supersaturation in hyperalkaline fluids (calcite avg. SI: 1.4 and aragonite avg. SI: 1.2; Fig. 9a and b) than in river waters (calcite avg. SI: 0.8 and aragonite avg. SI: 0.6; Fig. 9a and b). Dolomite [$CaMg(CO_3)_2$] is supersaturated in river waters (avg. SI = 2.5; Fig. 9c) and the majority of hyperalkaline fluids (avg. SI: 1.2; Fig. 9c). The BP5 pond water displays the highest SI values for calcite (1.8), aragonite (1.7), and dolomite (5). Magnesite [$MgCO_3$] is

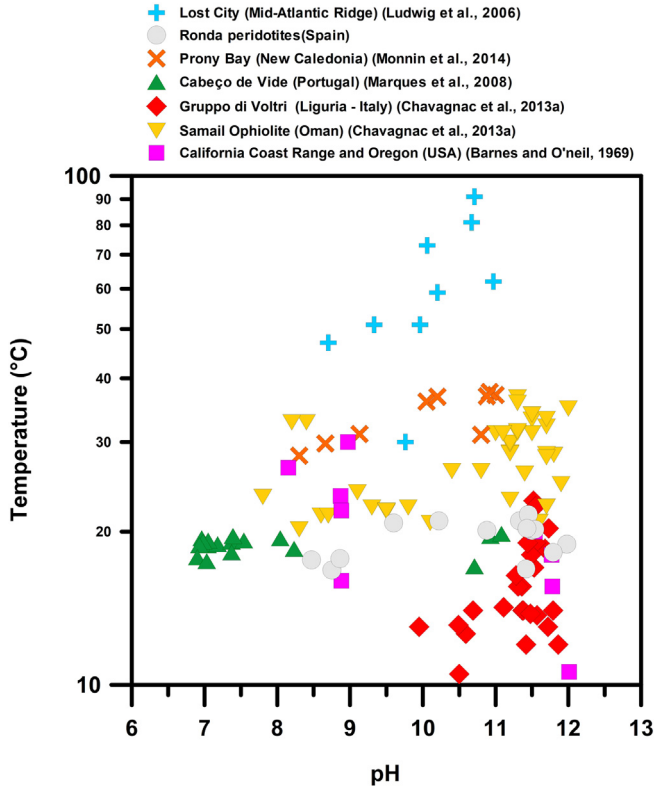

Fig. 5. Plot of the temperature versus pH of various serpentinite-hosted alkaline fluid sites worldwide.

supersaturated in the BP5 pond (2.5) and river waters (1.2) (Fig. 9d), while is undersaturated in the hyperalkaline fluids (Fig. 9d). The hydrated magnesium carbonate phases nesquehonite [$MgCO_3 \cdot 3H_2O$] and artinite [$Mg_2(CO_3)(OH)_2 \cdot 3H_2O$] are generally undersaturated in the hyperalkaline fluids and river waters (average SI < −1.5; Fig. 9e and f) except for fluids from the BP2 —supersaturated in artinite— and BP5 sites —supersaturated

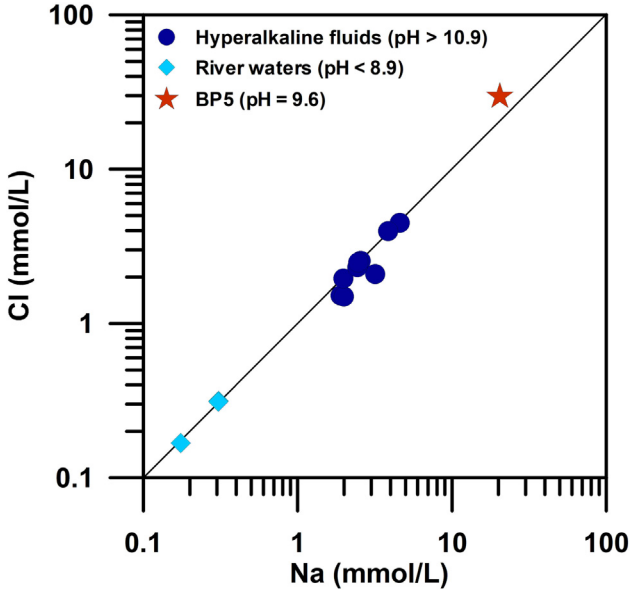

Fig. 6. Na vs. Cl diagram defining the different water types around the evaporation line.

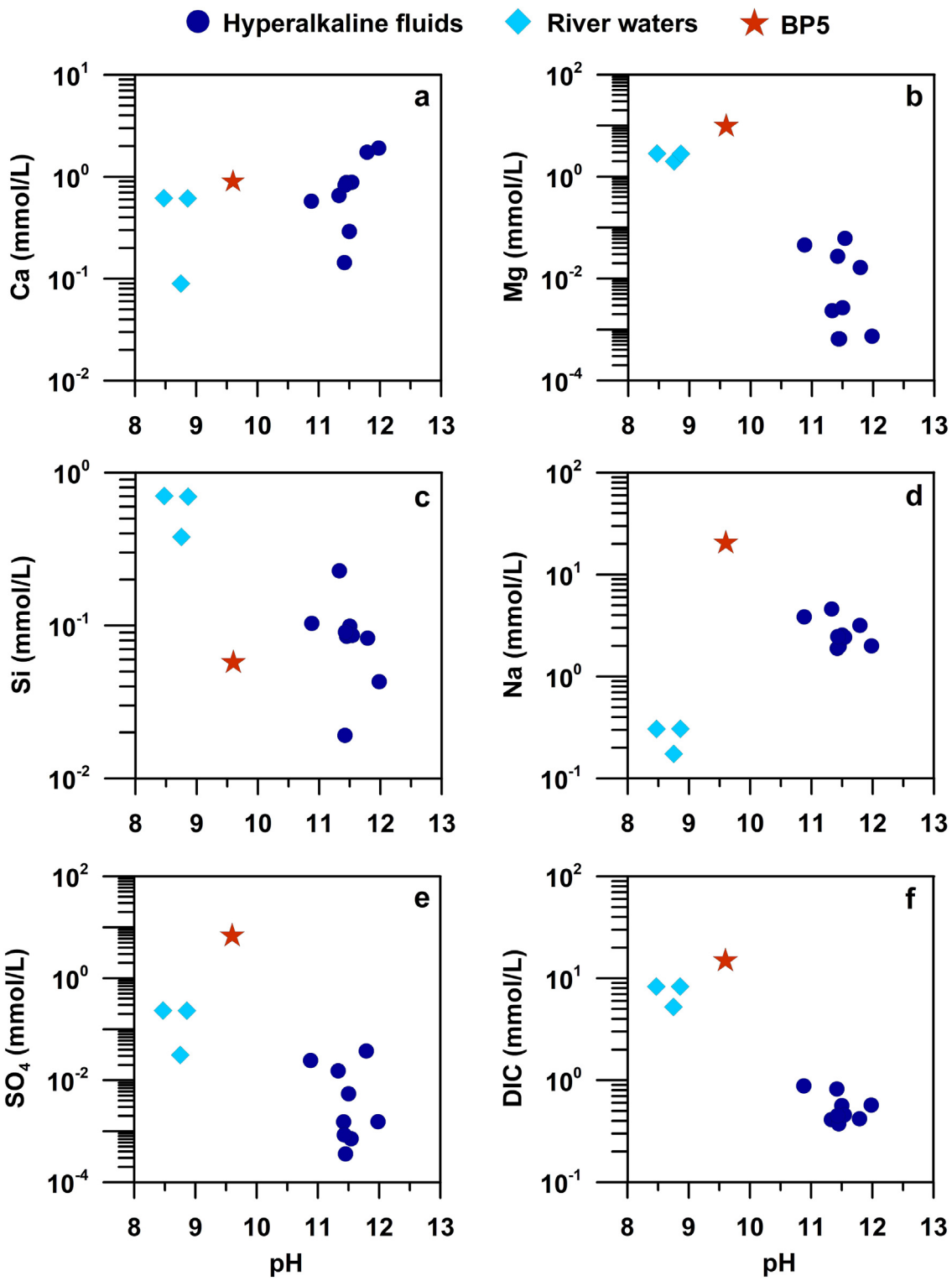

Fig. 7. Major element concentrations plotted against pH for the different water types in Ronda spring sites.

in nesquehonite and artinite— (Fig. 9e and f). Brucite [$Mg(OH)_2$] is supersaturated (Fig. 9g) in hyperalkaline fluids that exhibit the highest Mg concentrations (BAL, AMAR, and BP2 sites; [Mg] > 10^{-2}) (Table 2; Fig. 7b), and slightly undersaturated in the rest of the hyperalkaline fluids, and in the river waters and BP5 pond waters (Fig. 9g). Quartz is saturated in river waters (average SI of 0.8) and unsaturated in the hyperalkaline and BP5 fluids (Fig. 9h).

Altogether, the calculated pCO_2 for Ronda alkaline waters is negatively correlated with pH (Fig. 10). River water pCO_2 values reflect equilibration with the atmosphere, while hyperalkaline fluids show lower pCO_2 values in disequilibrium with the atmosphere. The pCO_2 of the BP5 pond water (−3.96 bar) is intermediate between those of river waters and hyperalkaline fluids (Fig. 10), indicating conditions closer to atmospheric equilibrium.

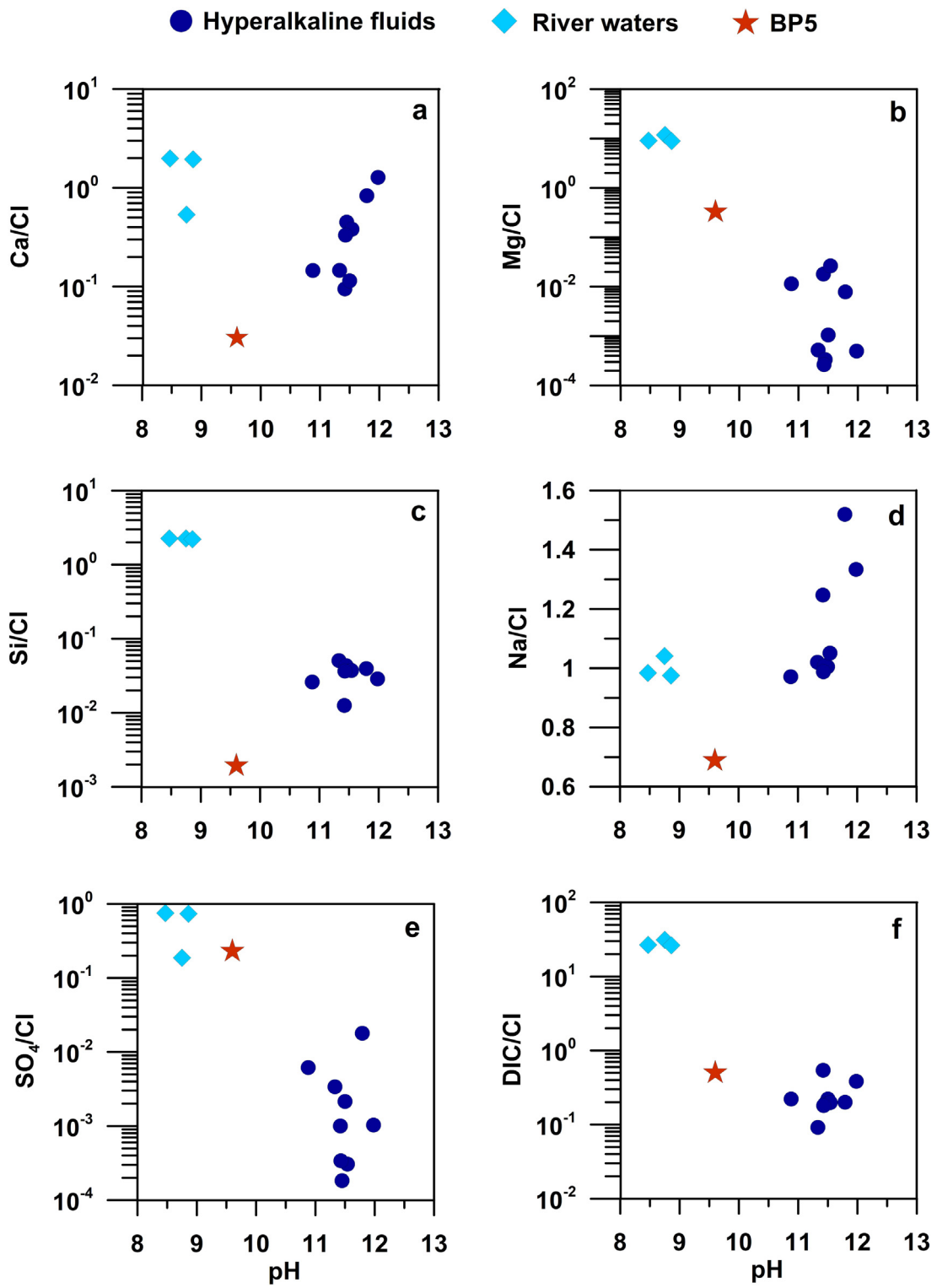

Fig. 8. Cl-normalized major element concentrations plotted against pH for the different water types in Ronda spring sites.

6.4. *Mineralogy and textures of precipitates*

Minerals identified the Ronda spring sites are mainly calcite and aragonite, and minor dolomite and Mg-Al-rich clays (Table 3). Other minerals (e.g., serpentine group minerals and quartz) (Table 3) are likely detritus.

6.4.1. *HED, AMAR, BAL and ALF sites*

Calcite is the predominant or single phase (Table 3) in travertine formed by hyperalkaline fluids at the HED, AMAR and ALF sites (Fig. 1b). Rhombohedral calcite (up to 60 μm) at the HED site shows poor crystallinity due to cementing processes (Fig. 11a). In the BAL site (Fig. 1b), aragonite exhibits dumbbell, cruciform, and spindle-like morphologies (Fig. 11b). Calcite is the main mineral of crystalline crusts where it forms aggregates of euhedral to subhedral {104} crystals (10 – 60 μm crystal size) that grow laterally to the air-water interface (Fig. 11c). A three-dimensional growth of calcite crystals takes place at the crust-water interface, while the crust side facing

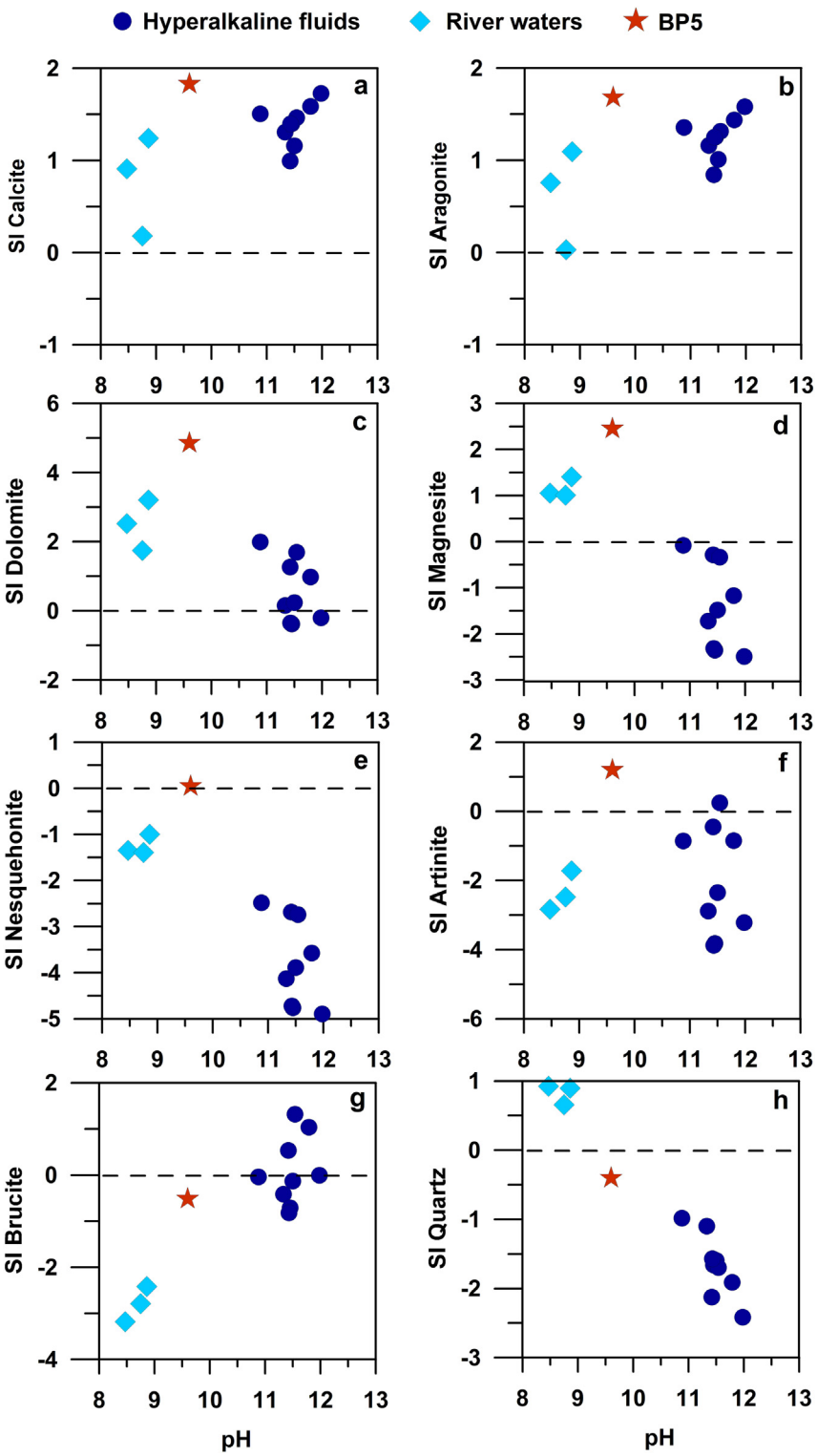

Fig. 9. Saturation indices (SI) versus the pH of potentially occurring minerals in different water types of Ronda spring sites. Horizontal dashed black line indicates the equilibrium state (SI = 0).

the atmosphere is flat due to non-occurring crystallization. (Fig. 11c). Minor branched, spindle aragonite crystals (Fig. 11d) are also present in the crust at the ALF site. The aragonite crystal size (10 – 20 μm) is relatively constant in all solid samples (cf. Section 3).

6.4.2. Baños del Puerto

Samples from the BP site contain variable proportions of calcite and aragonite, with calcite ratio ranging from 35 to 100%. Travertines at the hyperalkaline fluid discharging sites are mostly composed of calcite (Fig. 2b; Table 3) with chaotic and colloformic textures (Fig. 12a) typical of the onset of travertine formation (Pentecost, 2005). Travertines formed at the mixing sites of hyperalkaline fluids and river waters (Fig. 2a, c & d; Table 3) are rich in aragonite with spherulite morphologies (up to 100 μm in

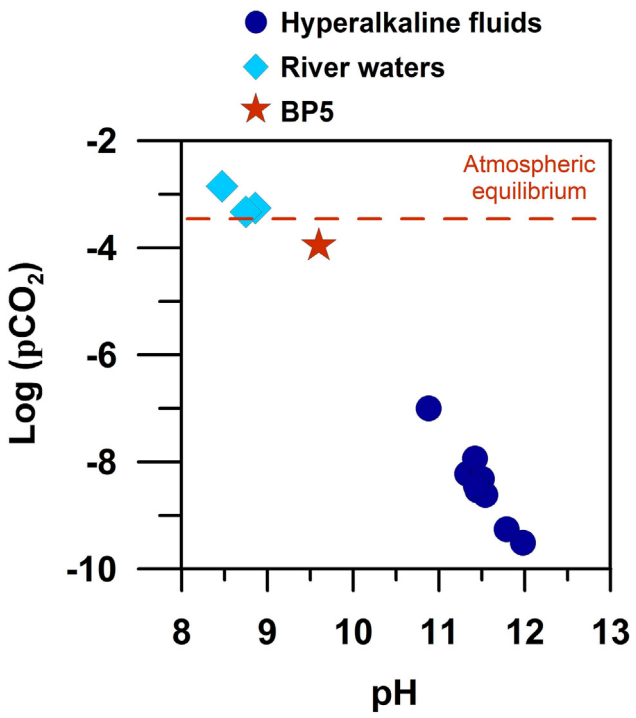

Fig. 10. Calculated pCO_2 versus the pH of different water types in Ronda spring sites. Horizontal dashed red line represents the point at which the waters are in equilibrium with Earth's atmosphere (pCO_2: −3.42 bar). (For interpretation of the references to color in this figure legend, the reader is referred to the Web version of this article.)

diameter) (Fig. 12b). Aragonite in the BP site is associated with Mg-Al-rich clays, possibly vermiculite (Fig. 12c). Dolomite is a minor component of lithified travertines, and a major phase in the BP5 pond (Fig. 2e) where it occurs as euhedral crystals up to 300 μm in size in sediments with Mg-rich cores overgrown by Ca-rich rims (Fig. 12d).

7. Discussion

In order to better constrain the carbonation processes in the Ronda continental serpentinite-hosted alkaline fluids, we will first discuss the processes accounting for the physico-chemical composition of the Ronda river waters and hyperalkaline fluids in the light of those already proposed for other continental serpentinite-hosted alkaline springs worldwide. We will then address the origin of the mineralogical and textural diversity of their associated mineral precipitates, and how it relates to the (hydro)dynamics of the Ronda alkaline spring systems.

7.1. Genesis of alkaline and hyperalkaline waters in the Ronda peridotites

7.1.1. Genesis of Ronda Mg–HCO_3 river waters

The relative enrichment of Ronda river waters in Mg and Si is characteristic of river waters running through serpentinites (Baumeister et al., 2015; Margiotta et al., 2012). Like surface alkaline waters in ophiolites worldwide (e.g., Barnes and O'Neil, 1969), the genesis of Ronda Mg–HCO_3 river waters is most likely due to hydrolysis of ferromagnesian peridotite minerals by the infiltration of meteoric water and shallow groundwater in equilibrium with the atmosphere following reactions such as (e.g., Paukert et al., 2012):

$$Mg_2SiO_4 + 4\,CO_2\,(g) + 2\,H2O \rightarrow 2Mg^{2+}\,(aq) + 4\,HCO_3\,(aq) + SiO_2\,(aq) \quad [3]$$

Percolation reaction path modelling of freshwater and rainwater through serpentinite under atmospheric CO_2 conditions demonstrates that this type of mineral hydrolysis reactions increases the concentration in Mg and H_4SiO_4 and, to a lower extent, the pH of water leading to mildly alkaline (pH > 8) Mg–HCO_3-rich waters (e.g., Bruni et al., 2002; Marques et al., 2008; Palandri and Reed, 2004; Paukert et al., 2012). Similarly, Mg–HCO_3 river waters in the Ronda peridotites are most likely generated by shallow chemical weathering of serpentinized peridotites by meteoric waters equilibrated with atmospheric CO_2 and O_2. The correlation of alkalinity with DIC concentrations in the Ronda river waters (Fig. 13 indicate that carbonic species (i.e., HCO_3^-) are the main source of alkalinity in agreement with a shallow circulation and interaction of these waters with vegetation and the atmosphere. The Cl-normalized alkalinity of the Ronda river waters is conservative relative to Cl-normalized Ca, K and Na (Fig. 14), which likely reflects that they are in equilibrium with Ca, K, and Na bearing minerals such as Ca-carbonates and clays.

Despite being saturated in $CaCO_3$, Mg-carbonates, and quartz, the Ronda river waters lack any precipitates of these minerals (Fig. 9a, b, c, d & h). The absence of calcite in $CaCO_3$-supersaturated water is common in Mg–HCO_3 waters worldwide (e.g., Lu et al., 2000; Pentecost, 1992; Suarez, 1983) and usually attributed to inhibited nucleation of $CaCO_3$ due to high fluid flow, short resident times, and high sediment loads (Rogerson et al., 2014; and references therein). Under moderate atmospheric pressure and ambient temperature, the abiotic formation of anhydrous magnesium carbonates is kinetically hindered (e.g., Arvidson and Mackenzie, 1999; Land, 1998), accounting for the lack of magnesite and dolomite in Ronda river waters.

Table 3
Location, description and mineralogy of solid samples.

Sample ID	Site	Sample description	Mineralogy (minor phases)
HED	Carratraca	White travertine precipitate from a pipe	Mg-calcite (vermiculite)
AMAR	Ronda	White travertine precipitate from human-made fountain	Calcite (aragonite)
BAL	Ronda	White sediment from the bottom of a water tank	Aragonite
ALF	Ronda	Travertine terrace around the hyperalkaline spring	Calcite (vermiculite)
ALF/SK	Ronda	Crystalline crust floating on water surface	Calcite (aragonite)
BP1	Ojén	Travertine terrace around human-made well	Calcite
BP1/SK	Ojén	Crystalline crust floating on water surface	Calcite
BP1/LI	Ojén	Lithified travertine terrace	Mg-calcite (dolomite, quartz, chrysotile, lizardite, unidentified clay)
BP2	Ojén	Yellowish travertine precipitate from human-made pond	Calcite
BP4	Ojén	Travertine terrace at the river bank	Mg-calcite (aragonite)
BP5	Ojén	Sediment from BP5 pond	Dolomite (aragonite, quartz, chrysotile, lizardite, unidentified clay)
BPR	Ojén	Travertine terrace before the river bank	Calcite, aragonite
BPR/CA	Ojén	Travertine terrace hanging over the river bank	Aragonite, calcite (dolomite, vermiculite)
BPR/IN	Ojén	Submerged travertine terrace in the river water	Aragonite, calcite (dolomite)

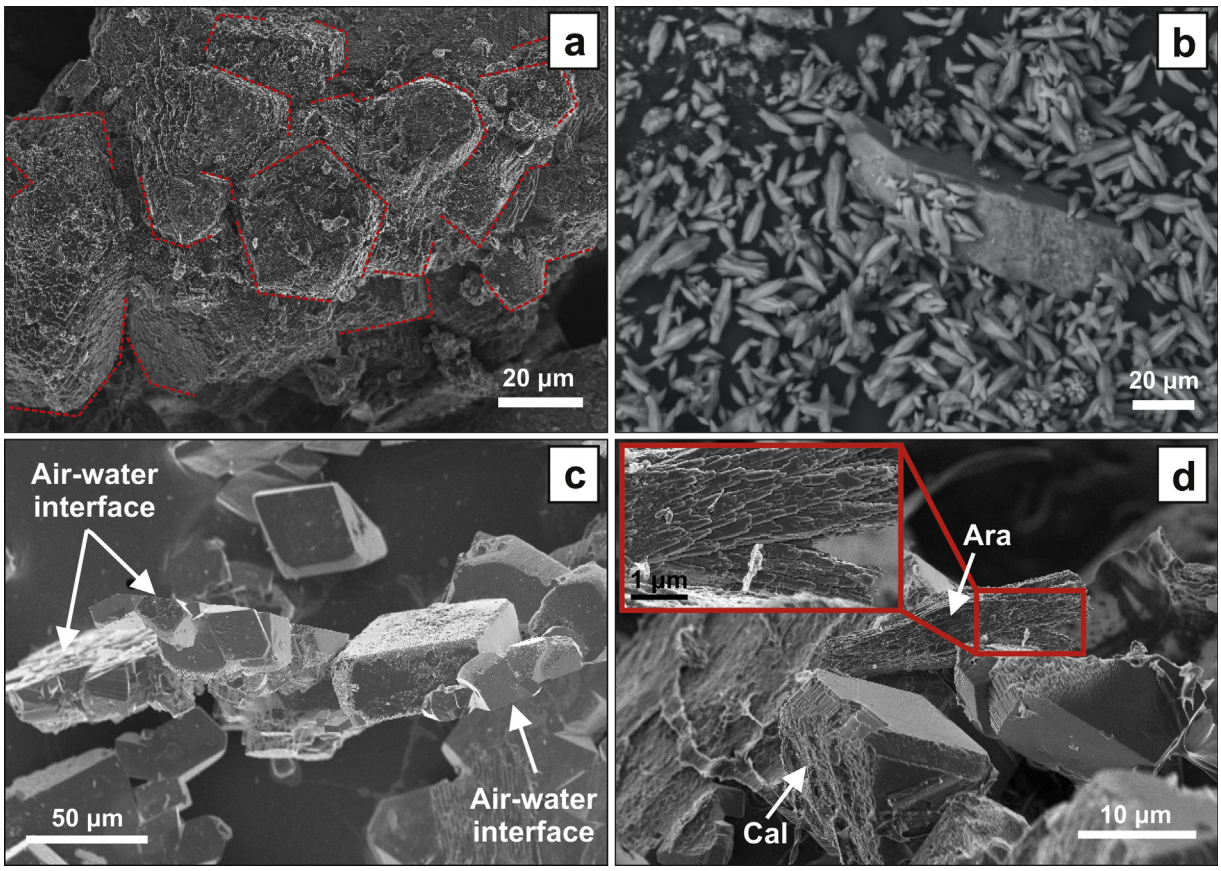

Fig. 11. Mineral phases and textures from HED, BAL and ALF sites. **a)** Sample of calcite-dominated travertine at the discharging site of HED spring site. Crystal boundaries (red dashed lines) of calcite get degraded due to lithification processes. **b)** Dumbbell, cruciform and spindle aragonite precipitating as sediment in BAL spring site. **c)** Calcitic crystalline crust forming at the air-water interface in ALF spring site. The side facing towards the air is flat, while calcite crystals grow towards the water column and exhibit euhedral {104} crystals. **d)** Calcite (Cal) -dominated crystalline crust with minor aragonite (Ara) amounts from ALF site. **Inset:** Zoom in the branching phenomenon of aragonite crystals. (For interpretation of the references to color in this figure legend, the reader is referred to the Web version of this article.)

7.1.2. Genesis of Ronda Ca–OH hyperalkaline fluids

7.1.2.1. Origin of hyperalkaline fluids by low-temperature serpentinization reactions. Ronda hyperalkaline fluids have physicochemical characteristics similar to other continental serpentinite-hosted Ca–OH hyperalkaline waters worldwide. The prevailing theory for the genesis of serpentinite-hosted, Ca–OH hyperalkaline fluids is that they form during low temperature serpentinization reactions driven by reactive percolation of meteoric Mg–HCO_3 surface waters in deep serpentine aquifers isolated from the atmosphere (Barnes and O'Neil, 1969; Boschetti and Toscani, 2004; Bruni et al., 2002; Kelemen and Matter, 2008; Neal and Stanger, 1985; Palandri and Reed, 2004). Among other reactions, the hydration of olivine and pyroxene by fresh water in a closed system to atmospheric CO_2 (e.g., Palandri and Reed, 2004; Paukert et al., 2012):

$$4Mg_2SiO_4 + CaMgSi_2O_6 + 7H2O \rightarrow 3Mg_3Si_2O_5(OH)_4 + Ca_{2+}(aq) + 2OH^-(aq) \quad [4]$$

accounts for the hyperalkalinity and chemistry of Ca–OH hyperalkaline fluids (Boschetti and Toscani, 2004; Bruni et al., 2002; Neal and Stanger, 1985; Palandri and Reed, 2004).

However, there are still many uncertainties about reaction path mechanism, residence time, and source of serpentinite-hosted hyperalkaline waters (Bruni et al., 2002; Chavagnac et al., 2013b; Paukert et al., 2012). Despite their long residence time in deep serpentine aquifers, the sluggish reaction rate of serpentinization reactions below 100 °C (McCollom et al., 2016) may call into question that low-temperature serpentinization is the sole origin for Ca–OH hyperalkaline fluids, but no alternative reactions pathways have yet been proposed.

The chemical similarity of deep coastal aquifer waters in the nearby Marbella area with Ronda Mg–HCO_3 river waters (Argamasilla et al., 2017) and the old ^{14}C age of the DIC in Ronda hyperalkaline fluids (c. 3 ka; Etiope et al., 2016), suggest that infiltration of meteoric-derived Mg–HCO_3 river waters are the potential source of Ronda Ca–HCO_3 hyperalkaline fluids. Alternatively, Ca–HCO_3 waters from nearby karst aquifers in western Alpujárrides limestones (Fig. 1b) (Barberá and Andreo, 2015), may also be a potential source.

Fig. 15 shows the chemical trends of Mg, Ca and DIC modelled for non-reactive (this study; dashed green line in Fig. 15; see figure caption for further details) and reactive peridotite/serpentinite percolation (Paukert et al., 2012; dashed and continuous black line in Fig. 15) of meteoric waters isolated from the atmosphere. The calculated trends for reactive percolation reproduce accurately the variations of Ca and Mg observed in Ronda river waters and hyperalkaline fluids, supporting that Ronda waters may form by deep percolation reaction of meteoric waters isolated from the atmosphere. As in the Oman Ophiolite hyperalkaline springs, at high pH, the Ca concentration of Ronda hyperalkaline fluids is less than those predicted in the Paukert et al. (2012) model (Fig. 15a). The lower Ca concentration may be due to precipitation of Ca-bearing carbonates (calcite and dolomite) because they are supersaturated at high pH as shown in our non-reactive models.

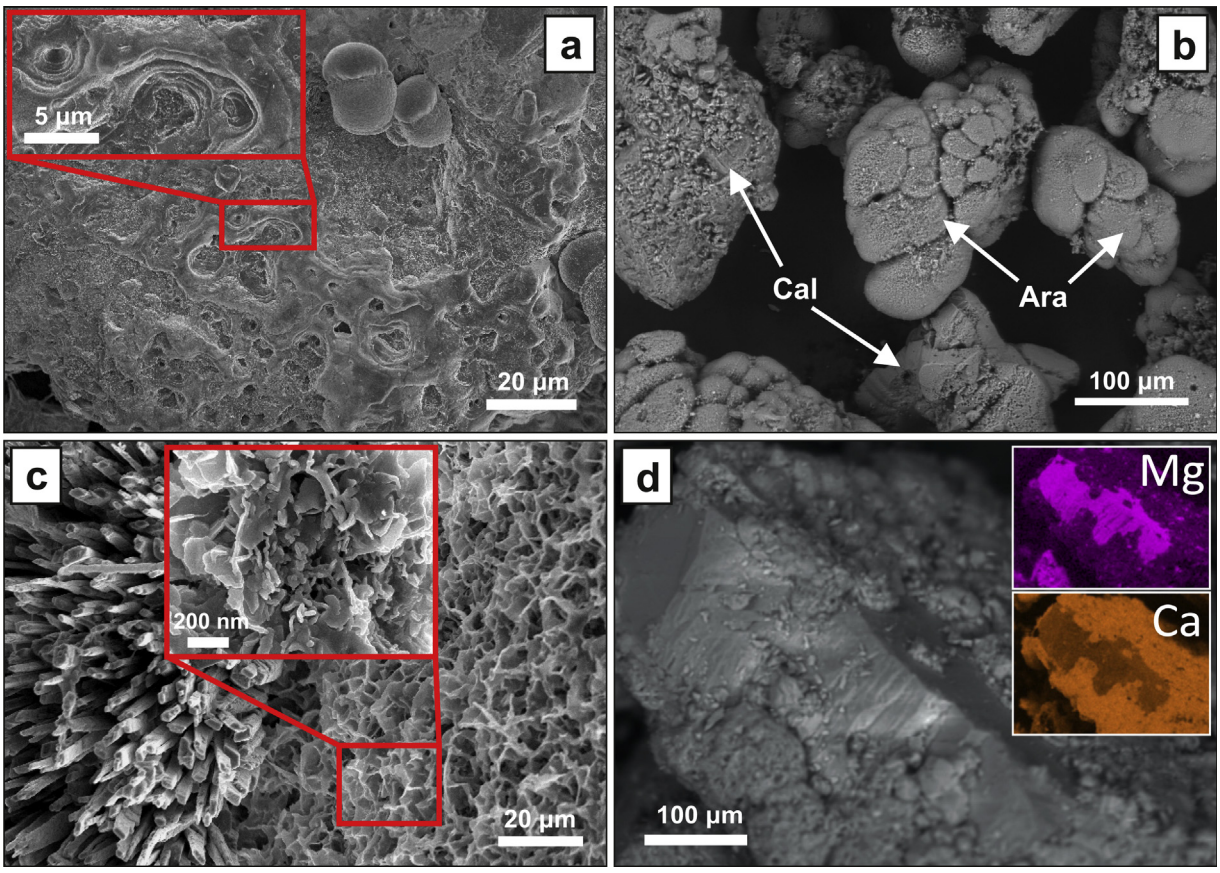

Fig. 12. Mineral phases and textures from BP site. **a)** Lithified travertine with chaotic morphologies due to precipitation from multiple fluid generations. **Inset:** Zoomed image of vugs and clefts with step that are dispersed over the carbonate layers. **b)** Sphere-like aragonite (Ara) co-existing with calcite (Cal) in submerged parts of travertine in river waters. **c)** Acicular aragonite rods growing in association with clay minerals. **Inset**: Zoomed image displays the interlocking flaky clay crystals. **d)** Aragonite growing on the surface of dolomite crystal in sediments of BP5 pond.

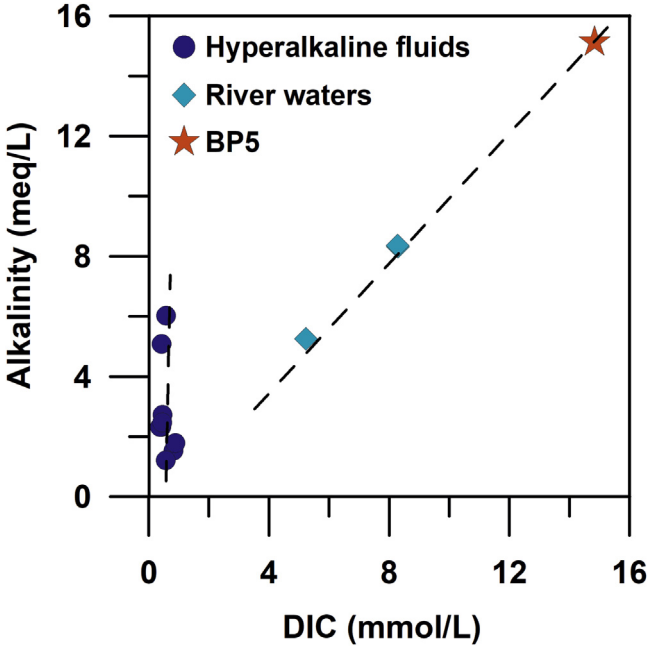

Fig. 13. Alkalinity versus DIC concentration of the different water types in Ronda spring sites. Dashed lines indicate the different trends between the water types based on the Alkalinity-DIC relationship.

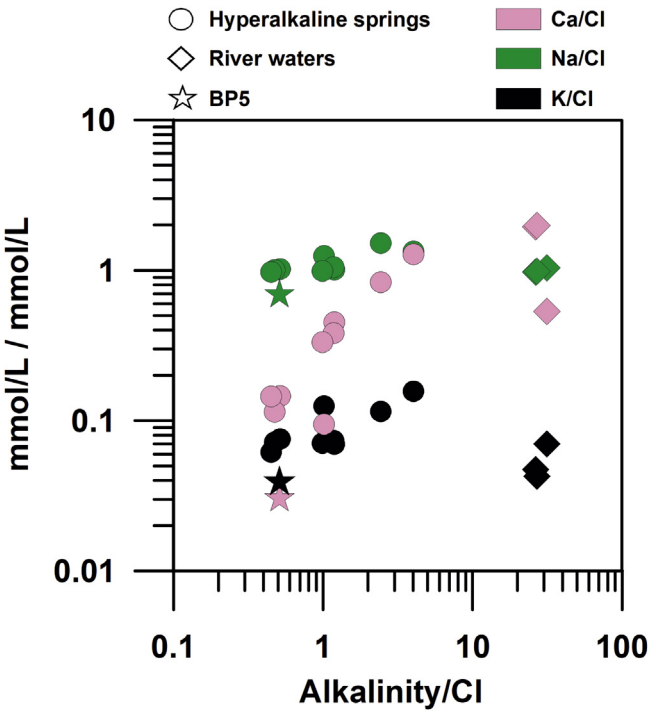

Fig. 14. Cl-normalized Ca, Na and K versus Cl-normalized alkalinity of the different water types in Ronda spring sites.

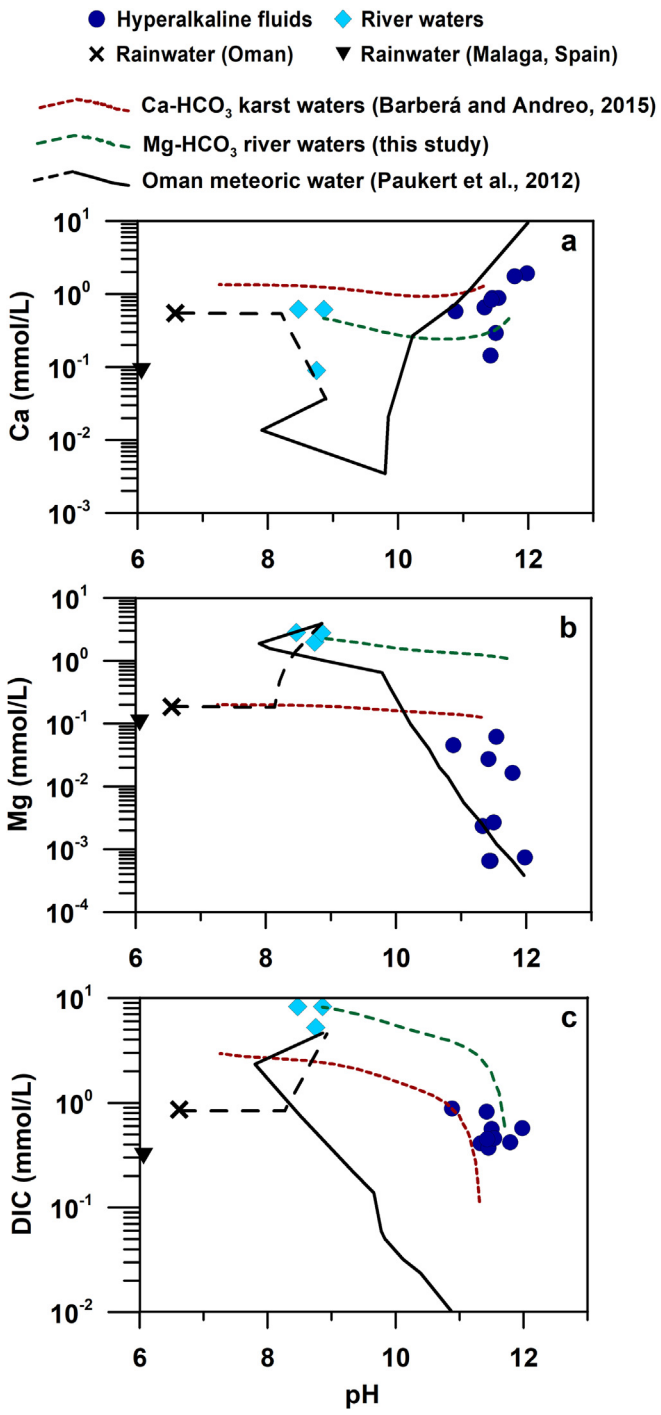

Fig. 15. Comparative graphs of non-reactive (this study) and reactive (Paukert et al., 2012) models of water isolation from the atmosphere. The graphs include **a)** Ca, **b)** Mg and **c)** DIC versus pH in natural water samples from Ronda peridotites. The red and green dashed lines indicate the aqueous species evolution under non-reactive isolation from the atmosphere of Ca-HCO_3 waters (Barberá and Andreo, 2015) and Mg-HCO_3 (green line, this study), respectively. Dashed black line indicates model reaction progress in an open system. Solid black line indicates reaction progress under a closed system. (For interpretation of the references to color in this figure legend, the reader is referred to the Web version of this article.)

Rempfert et al., 2017 reported higher Ca concentrations (> 3.5 mmoL/L) in hyperalkaline fluids collected from deep wells in the Oman Ophiolite (up to 475 m depth) than in hyperalkaline springs, indicating higher Ca at depth that has been decreased due to precipitation of Ca-rich carbonates in the shallow subsurface due to mixing with HCO_3-rich shallow groundwater (Neal and Stanger, 1985).

The increase in Mg concentration in the pH range of 7.5 − 8.5 observed in the Ronda and Oman alkaline springs (Fig. 15b) is likely caused by hydration of peridotite Mg-silicates (Eq. (4)) (Palandri and Reed, 2004; Paukert et al., 2012). The subsequent decrease in Mg concentration at increasing pH (Fig. 15b) is caused by the formation of hydrated Mg-bearing minerals —serpentine and brucite— during deeper fluid percolation (Palandri and Reed, 2004; Paukert et al., 2012).

Percolation reaction models greatly overestimated the observed decrease of the DIC from river waters to hyperalkaline fluids (Fig. 15c). The observed decrease in DIC is better accounted by non-reactive models due to the precipitation of Ca-bearing carbonates that become oversaturated at hyperalkaline pH (Fig. 15c). This process may also explain the formation Mg-rich carbonates (e.g., magnesite) veins in serpentinized-peridotite (Andreani et al., 2009; Bruni et al., 2002; Cipolli et al., 2004; Kelemen et al., 2011), as well as the potential formation of Ca-rich carbonates prior to fluid discharge and interaction with the atmosphere at the spring sites (Paukert et al., 2012).

The lack of correlation of alkalinity with DIC in Ronda hyperalkaline fluids is also observed in hyperalkaline fluids from the Troodos (Neal and Shand, 2002), Ligurian (Chavagnac et al., 2013b; Cipolli et al., 2004), Cabeço de Vide (Marques et al., 2008), Oman (Chavagnac et al., 2013b; Paukert et al., 2012), and Coastal Range (Barnes and O'Neil, 1971) ophiolites . In these ophiolites, the DIC of hyperalkaline fluids is extremely low as opposed to the DIC-rich nature of the mildly alkaline Mg-rich waters in the same ophiolite. The low pCO_2 of Ronda hyperalkaline fluids (Fig. 10) precludes that their DIC was acquired by equilibration with the atmosphere and indicates a deeper origin for their low DIC nature. Assuming they evolved from meteoric Mg—HCO_3 waters during percolation-reaction in deep serpentinite aquifers, the low DIC of the Ronda Ca—OH hyperalkaline fluids (Fig. 7f) is then most likely due to deep precipitation of carbonates.

In Ronda hyperalkaline fluids, Ca and, to a lesser extent, Na and K concentrations are positively correlated with the normalized alkalinity (Fig. 14). These correlations, together with the lack of correlation of alkalinity with DIC (Fig. 13), points to an OH-based alkalinity production coupled to the dissolution of Ca, Na, and K bearing minerals.

7.1.2.2. The source of Ca of hyperalkaline fluids. In the low-temperature serpentinization reaction hypothesis, the main Ca source of hyperalkaline fluids comes from the hydrolysis of peridotite anhydrous Ca-bearing silicates such as clinopyroxene, orthopyroxene, and plagioclase (e.g., Palandri and Reed, 2004). These phases are minor component of peridotites and are almost absent in residual (i.e., recording high extent of melting) peridotites such as harzburgite in the mantle section of the Oman Ophiolite. Subcontinental mantle peridotites, such as the Ronda peridotite, are more fertile (i.e., richer in Ca and Al) than their ophiolitic counterparts (Bodinier and Godard, 2006). In the Ronda peridotites, Ca-silicates occur in lherzolites and harzburgites, wehrlite patches in dunites, pyroxenite layers, and rare intrusive gabbros (Garrido and Bodinier, 1999; Hidas et al., 2013b, 2015; Lenoir et al., 2001; Obata et al., 1980; Tubía, 1994; Varas-Reus et al., 2018).

Fig. 16 shows the volume of reacted peridotite that accounts for the yearly amount of Ca discharged in hyperalkaline springs. The mass balance assumes that the total consumption of Ca by chemical weathering of Ca-bearing minerals in residual (dunite with 0.5 CaO wt%) to fertile (lherzolite with 4.0 CaO wt%) peridotite, is 1 mmoL/L with a flow rate of $4.73 \cdot 10^5$ L/y per spring. The mass balance indicates that weathering of 0.21 m^3 of fertile lherzolite —or 1.68 m^3 of residual dunite— is required to account for the mass of Ca

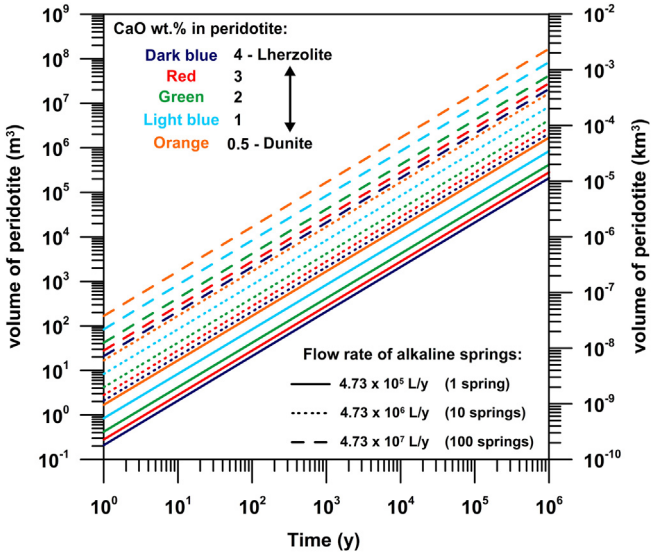

Fig. 16. Estimation of the reacted volume of peridotite (in m^3 and km^3) as a function of time under different CaO wt% and flow rates. Dark blue and orange color corresponds to lherzolite (4 CaO wt%) and dunite (0.5 CaO wt%) rock composition, respectively. Red, green and light blue colors correspond to intermediate rock compositions between 0.5 and 4 CaO wt%. (For interpretation of the references to color in this figure legend, the reader is referred to the Web version of this article.)

discharged yearly by one hyperalkaline spring (Fig. 16). Assuming a steady-state flow rate, the weathered volume of peridotite during the 3 ka residence time of these fluids in deep serpentinite aquifer (Etiope et al., 2016) is $6.3 \cdot 10^{-7}$ km^3 of fertile lherzolite or 5.1 10^{-6} km^3 of residual dunite (Fig. 16). This volume of peridotite corresponds only to c. $1.0 - 7.5 \cdot 10^{-7}$% of the total volume of the Ronda peridotites (c. 675 km^3; assuming a constant thickness of 1.5 km along the 450 km^2 of exposed peridotites; Fig. 1). The volume of water discharged yearly in Ronda hyperalkaline fluid springs is unknown; assuming a total of 100 alkaline springs with Ca concentration and flow rates similar to those investigated here, the mass of Ca discharged in Ronda hyperalkaline springs in 1 Ma requires weathering of 0.003% or 0.025% of the total volume of the Ronda lherzolite and dunite, respectively. These are upper bound estimates as hyperalkaline fluids derive from meteoric waters that already contained Ca (Fig. 15a and b). The computation indicates that weathering (i.e., hydrolysis; Eq. (4)) of Ca-silicates in the Ronda peridotites is a viable source to account for Ca concentration in hyperalkaline springs. However, it implies a steady-state dissolution rate of clinopyroxene of $1.6 \cdot 10^{-12}$ moL/$cm^2 \cdot s$ (considering an average clinopyroxene grain size of 100 μm; Vauchez and Garrido, 2001) that is about eight order of magnitude faster than experimental values for steady-state dissolution rates of dissolution of Ca-rich pyroxene (c. $10^{-20} - 10^{-19}$ moL/$cm^2 \cdot s$ in the ranges of 20 – 100 °C and 6 < pH < 7; Zhang et al., 2013).

De Obeso and Kelemen (2018) have shown that limestones can be an alternative source of Ca in some Oman Ophiolite hyperalkaline springs. An alternative source of Ca for the Ronda hyperalkaline fluids could be limestone karst aquifers (Sierra Blanca and Sierra de las Nieves) surrounding the Ronda peridotite massifs (Fig. 1b). Karst aquifers near the Ronda peridotite spring sites show the highest annual rainfall (> 800 mm), recharge (400 – 700 mm/y) and infiltration coefficient (40 – 70%) in the Betic Cordillera (Martos-Rosillo et al., 2015). These karst aquifers host Ca–HCO_3 waters that may infiltrate the peridotite along serpentinite-rich faults and become the source of the Ronda Ca–OH hyperalkaline fluids (Fig. 15).

7.1.2.3. Genesis of methane bubbling in the spring sites. Methane —bubbling in springs, ponds, and rivers (Fig. 2a)— is the main gas emitted in some of the Ronda peridotite hyperalkaline sites (Etiope et al., 2016). Methane is the dominant gas in serpentinite-hosted hyperalkaline springs in most continental peridotites (e.g., Etiope and Whiticar, 2019; and references therein), but hydrogen is dominant in some such as the Oman Ophiolite hyperalkaline spring. Etiope et al. (2016) analyzed the C and H stable isotope composition of gases emitted from several Ronda hyperalkaline springs. They concluded that methane was predominantly abiotic and was genetically unrelated to the water DIC that has a younger ^{14}C age than methane (Etiope et al., 2016). Dating of $^{14}C - CH_4$ in serpentinite-hosted hyperalkaline springs systematically shows that methane carbon is several thousands of years older than the DIC ^{14}C ages —hundred to thousand years— dating the residence time of water in the aquifer (Cipolli et al., 2004; Marques et al., 2008; Etiope et al., 2016; Etiope and Whiticar, 2019). Hypotheses proposed for the origin of abiotic methane in serpentinite-hosted hyperalkaline springs include gas-phase CO_2 hydrogenation (Sabatier's reactions) (Etiope and Sherwood Lollar, 2013; Etiope and Whiticar, 2019; McCollom, 2016; and references therein), and a deep magmatic or hydrothermal source (De Boer et al., 2007; Grozeva, 2018).

7.2. Mineralization and mineral textures in Ronda hyperalkaline springs

7.2.1. Travertine

Like other continental serpentinite-hosted alkaline springs (e.g., Chavagnac et al., 2013a & b; Neal and Stanger, 1984; Paukert et al., 2012; Stanger, 1987), travertines in the Ronda peridotites occur around the discharging sites of hyperalkaline fluids, along their flow paths, and at the mixing sites of these waters with Mg–HCO_3 river waters (Fig. 2a and d). In the Ronda peridotites, the different stages and mechanisms of travertine formation are well illustrated in the BP spring site (Figs. 2 and 17). Although aragonite and calcite are supersaturated in the BP hyperalkaline fluids (Fig. 9 a & b), calcite is the only $CaCO_3$ polymorph present in travertine at the discharging sites (Fig. 2b; Table 3). Aragonite is occasionally observed in the crystalline crusts that form in the ponds near the discharging sites (Section 6.4.2). Precipitation of calcite upon uptake of atmospheric CO_2 is commonplace in hyperalkaline spring fluids with low Mg/Ca ratio (< 0.5) and T < 40 °C (Folk, 1994; Jones, 2017a; Pentecost, 2005, and references therein) such as those around the Ronda spring discharging sites (Mg/Ca < 0.2, avg. T: 19.9 °C; Fig. 17a). The cause of the preponderance of calcite precipitation in Ca-rich and low Mg/Ca fluids is a matter of some debate (Jones, 2017a). Experimental studies show that aragonite forms at temperatures > 30 °C, while calcite is more stable at lower temperatures (e.g., Meldrum and Cölfen, 2008; Zeller and Wray, 1956). However, in natural settings, both $CaCO_3$ polymorphs precipitate in a wide range of temperature (Jones, 2017a). Degassing of CO_2 is the most common cause of travertine precipitation from $CaCO_3$-supersaturated fluids. Although rapid CO_2 degassing of CO_2-rich fluids promotes aragonite precipitation irrespective of their temperature and Mg/Ca ratio (e.g., Jones and Peng, 2016; Pentecost, 2005), degassing-induced aragonite precipitation is likely very limited in the Ronda hyperalkaline fluids because of their very low pCO_2 (Fig. 10).

A parallel mechanism for the formation of travertine in the Ronda spring sites is carbonate precipitation by mixing of Ca–OH-rich hyperalkaline fluids with Mg–HCO_3-rich river waters (Fig. 17b and c). In the BP site the aragonite content of travertines gradually increases towards the riverside pointing to the mixing of Ca–OH-rich hyperalkaline fluids with Mg–HCO_3-rich river waters as the driving force for aragonite precipitation in this spring site (Fig. 17b and c). The nature of $CaCO_3$ polymorph that precipitates also depends on Mg content and Mg/Ca ratio of the fluid; Mg ions suppress

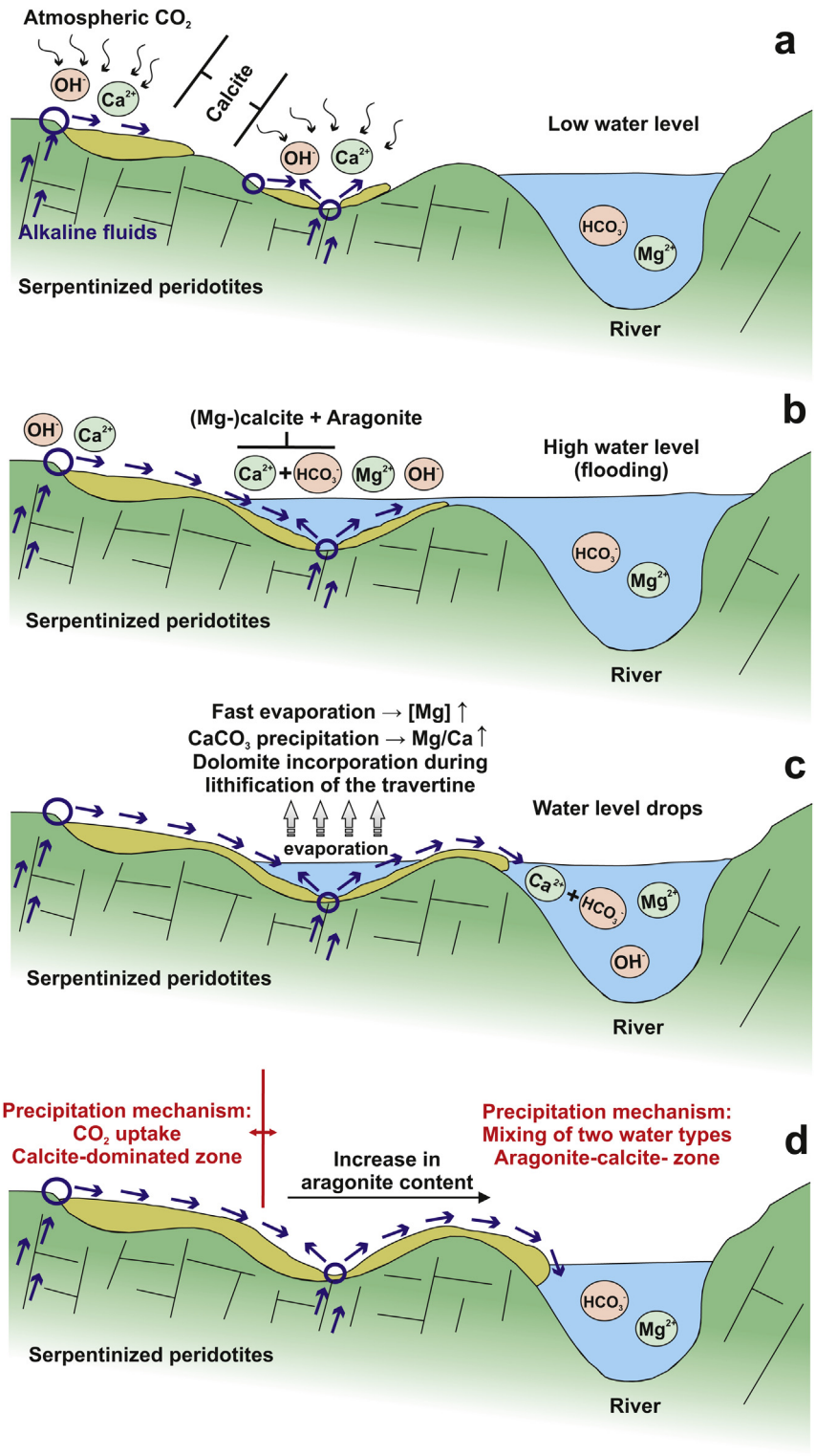

Fig. 17. Conceptual model of carbonate mineral precipitation during fluctuations of the river water level. **a)** Hyperalkaline fluids form calcite-dominated travertine due to atmospheric CO_2 uptake upon discharge. **b)** Flooding events of river water overflows the formed travertine. Aragonite and (Mg-)calcite precipitate as a result of the mixing of the two fluids. **c)** Fast evaporation leads to dolomite formation during travertine lithification processes. Water level retreats, and mixing processes continue to take place along the river bank forming travertine. **d)** Two zones of different precipitation mechanisms can be observed; i) precipitation due to CO_2 uptake leading to calcite-dominated travertine around the discharging sites of hyperalkaline fluids, and ii) travertine enriched in aragonite due to mixing of the two water types as the river is approached. The straight blue, undulating black and dashed grey arrows correspond to the hyperalkaline fluid flow paths, CO_2 uptake and evaporation, respectively. (For interpretation of the references to color in this figure legend, the reader is referred to the Web version of this article.)

the transformation of metastable $CaCO_3$ phases to calcite (Kitamura, 2001; Reddy and Wang, 1980) while higher Mg/Ca ratios favor aragonite precipitation (Burton, 1993; Falini et al., 1994; Lin and Singer, 2009). In the BP site, the increasing content in aragonite in travertine towards the riverside indicates that the main driver for aragonite precipitation is likely secular variations in the fluid Mg/Ca ratio likely due to seasonal flooding of the springs by the Mg–HCO_3 river waters and mixing with Ca–OH hyperalkaline spring fluids (Fig. 17b–d).

Textures of $CaCO_3$ minerals in the BP travertines support fast supersaturation rates as expected by sudden changes in the fluid Mg/Ca ratio during secular flooding and water mixing. Polycrystalline aragonite with spherulitic, needle-like morphologies in BP travertines (Fig. 18a) is consistent with experimental and natural crystallization under high supersaturation states (Fernandez-Diaz et al., 1996; Jones, 2017b). In some instances, aragonite displays non-classical crystal growth textures that are consistent with growth by oriented aggregation of nanoparticles (Fig. 18b). During this process, $CaCO_3$ particles — probably amorphous— are self-assembled at the tips of the crystals, leading to a two-dimensional lateral reorganization on the surface of the previous flattened particle (Beniash et al., 1997; De Yoreo et al., 2015) (Fig. 18b).

7.2.2. Crystalline crusts and sediment deposits

Precipitation of crystalline crusts upon discharge is common in serpentinite-hosted alkaline springs (e.g., Oman Ophiolite alkaline springs; Chavagnac et al., 2013a; Paukert et al., 2012). In Ronda alkaline springs, crystalline crusts — mostly composed of calcite— only occur in hyperalkaline ponds and discharging fluid sites (Section 6.4) (Fig. 11c). Calcite-dominated travertine in the Ronda hyperalkaline discharging sites and calcite floating crusts are formed by the precipitation of calcite upon uptake of atmospheric CO_2 by the hyperalkaline fluids. Flat-faced rhombohedral {104} and curved edges in calcite (Fig. 11c) indicate, respectively, events of slow and fast growth due to changes in supersaturation rate (Pope and Grotzinger, 2000). This variability in calcite morphology likely records spatial and temporal fluctuations in the supersaturation rate modulated by the supply of atmospheric CO_2 and the evaporation rate. The homocentric cavities in calcite surfaces may record that methane gas bubbles were attached during the growth of calcite clusters (Fig. 18c) (Taylor and Chafetz, 2004; Aquilano et al., 2003). Alternatively, they might be due to microbial activity (e.g., cyanobacteria) during calcite precipitation (Martinez et al., 2010; Bundeleva et al., 2014).

The BAL, AMAR, and HED sites do not display the natural hydrological features of the ALF and BP site, and we investigated travertine, crystalline crusts and sediments only at the discharging sites. Calcite is the only carbonate phase in AMAR and HED sites, probably because of the absence of river waters as a Mg source. The BAL spring is aragonite-dominated, which is in agreement with the elevated Mg content and high Mg/Ca ratio of these fluids relative to other hyperalkaline springs. Aragonite crystals in the BAL site show branching features (Fig. 11d) that may be indicative of high supersaturation level and fast supersaturation rates (Fernandez-Diaz et al., 1996) and may record sudden changes in the Mg-content of fluids at this spring site.

7.2.3. Formation of dolomite in travertine and sediments

In Ronda, dolomite occurs in the aragonite-bearing travertine at

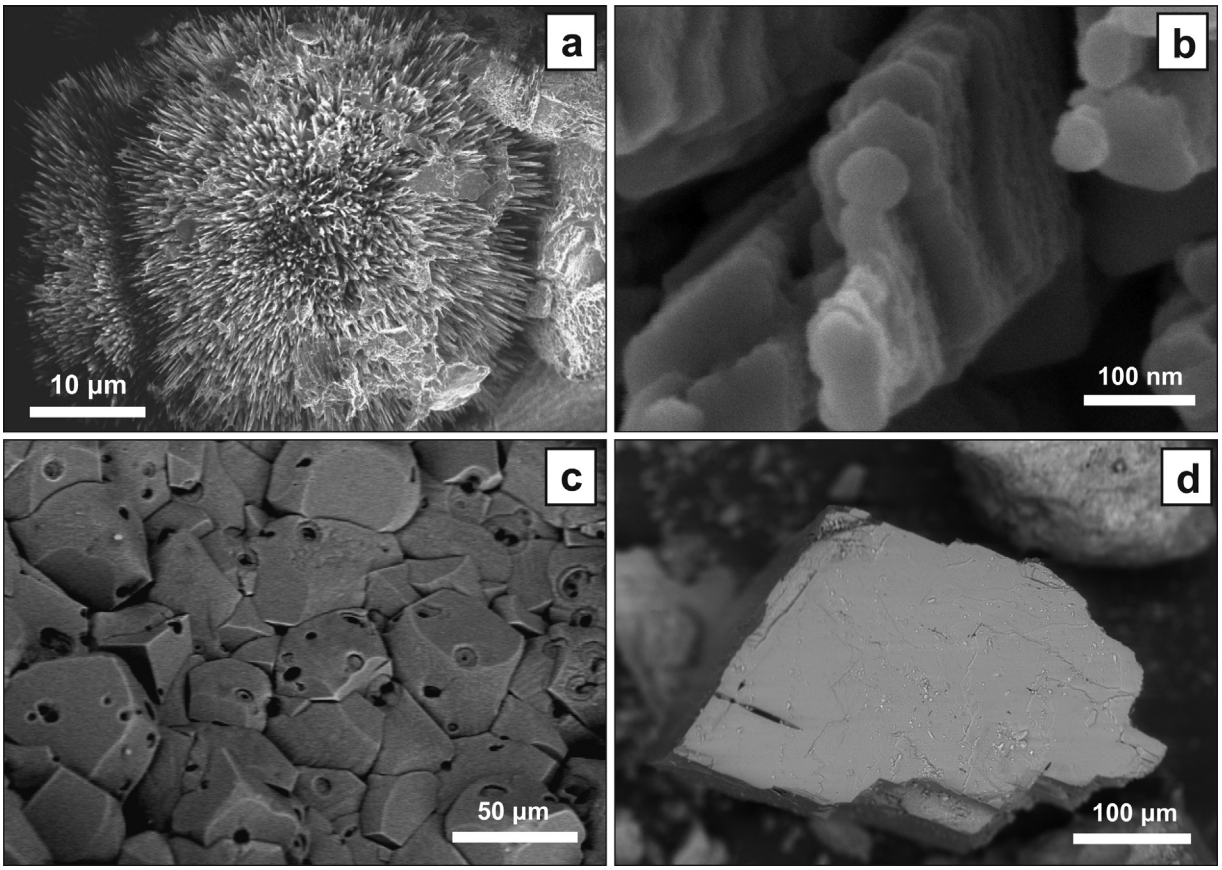

Fig. 18. Textural characteristics of mineral phases in BP site. **a)** Polycrystalline aragonite with spherulitic, needle-like morphology in BP travertine. **b)** Nano-rods of aragonite formed by aggregation of flat nano-particles with a thinning towards the tip of the crystal. **c)** Holes on calcite surface indicating the presence of gas bubbles. **d)** Large, euhedral dolomite crystal showing strong crystallographic symmetry.

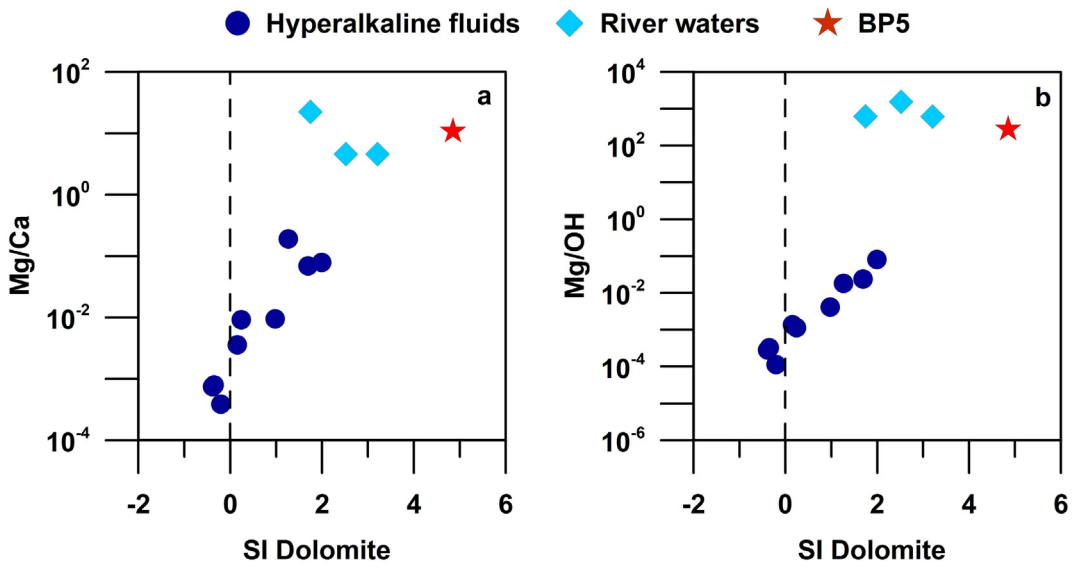

Fig. 19. **a)** Mg/Ca and **b)** Mg/OH versus dolomite saturation index (SI) of the different water types in Ronda spring sites. Vertical dashed black line indicates the equilibrium state (SI = 0).

BP site (Table 3) formed by mixing of Ca–OH hyperalkaline fluids with Mg–HCO_3 river waters (Fig. 17b and c). Several authors have reported variable amounts of dolomite in lithified travertines associated with serpentinite-hosted alkaline fluids (Barnes and O'Neil, 1971; Mervine et al., 2014; Renaut and Jones, 1997), where dolomite forms from trapped pore water with high Mg/Ca during lithification and early diagenesis (Fischbeck and Muller, 1971; Folk, 1993; Renaut and Jones, 1997).

Dolomite is absent in most of the investigated sediments in alkaline ponds (Table 3); a remarkable exception is the sediments from the BP5 pond (Fig. 2e) that contain c. 90% dolomite. The elevated S and P concentrations in BP5 pond may be indicative of microbial activity, opening the possibility of dolomite precipitation by bacterial sulfate reduction (e.g., Vasconcelos et al., 1995), methanogenesis (e.g., Roberts et al., 2004), or sulfate-driven anaerobic oxidation of CH_4 (e.g., Boetius et al., 2000; Peckmann and Thiel, 2004). Such biotic processes may seem inconsistent with the oxidative environment of the BP5 pond, but biotic dolomite formation under aerobic and hypersaline conditions may take place at the water-sediment interface (Sánchez-Román et al., 2009). Biotic crystallization of dolomite is, however, unlikely because dolomite crystals exhibit classical crystal growth with symmetrical features (Fig. 18d) unlike the typical spherical or dumbbell morphologies of biotic dolomite crystallization (e.g., Sánchez-Román et al., 2009; Van Lith et al., 2003; Warthmann et al., 2005; Zhang et al., 2012).

The abiotic precipitation of large amounts of dolomite is uncommon at atmospheric conditions even in dolomite-supersaturated fluids (e.g., Land, 1998) such as most of the Ronda alkaline fluids (Fig. 9c). The supersaturation of dolomite in BP5 pond is expected, as this pond shows the highest Mg and DIC concentrations (Fig. 7b and f), as well as elevated Ca concentrations compared to river waters (Fig. 7a). Indeed, BP5 pond displays the highest supersaturation in dolomite (Fig. 9c) compared to river waters and hyperalkaline fluids. Thermodynamic calculations suggest that despite the very low Mg concentrations ($min = 2.35 \times 10^{-6}$ mmoL/L) in hyperalkaline fluids, dolomite reaches supersaturation when Mg/Ca ratio in the fluids is over 3.6×10^{-3} (Fig. 19a), and Mg/OH ratio is over 1.1×10^{-3} (Fig. 19b). Dolomite in pond BP5 sediments points that fluids are already highly supersaturated in dolomite before their discharge at the pond (Badiozamani, 1973). In BP5 pond, the values of pH, Cl-normalized Mg, and DIC fall between those of hyperalkaline fluids and river waters, showing characteristics of both water types. Thus, possible subsurface mixing of Ca–OH hyperalkaline fluids and shallow Mg–HCO_3 waters might induce dolomite supersaturation before discharge.

Alternatively, the formation of dolomite could be favored under conditions of high salinity (Orr Chazen and Ehrlich, 1973; Vasconcelos and McKenzie, 1997) or changing-salinity environments such as sabkhas (Müller et al., 1990). The very high conductivity (Fig. 4b) and Cl^- concentrations (Fig. 6) show that BP5 pond underwent high evaporation rates that could inhibit Mg ion hydration and promote dolomite precipitation under atmospheric conditions (Di Tommaso and de Leeuw, 2010). Furthermore, high alkalinity and conductivity of BP5 pond fluids (Fig. 4b and c) decrease the low-temperature kinetic barrier for dolomite precipitation (Sánchez-Román et al., 2009). Roberts et al. (2013) demonstrated that natural surfaces possessing a high density of carboxyl groups might be a mechanism by which abiotic dolomite nuclei forms. Roberts et al. (2013) suggested that carboxyl group formation is accelerated in environments of changing or high salinity, meteoric-saline water mixing, or in certain weathering settings (e.g., presence of clays). The physicochemical and hydrological characteristics of the BP5 pond seems to meet the conditions for low-temperature dolomite precipitation so long-hypothesized but rarely documented in nature.

8. Conclusions

Waters in the Ronda peridotite spring sites can be classified into hyperalkaline fluids and river waters that are, respectively, similar to the Ca–OH (i.e., Ca^{2+}–OH^--rich) and Mg–HCO_3 (i.e., Mg^{2+}–HCO_3^--rich) water types described in ophiolite-hosted alkaline springs elsewhere. Ronda hyperalkaline fluids are characterized by relatively high pH (10.9 – 12), low Mg and high Na, K, Ca, and Cl^- concentrations and occur in the discharge sites and in natural ponds formed along the flow path of discharging fluids. River waters are enriched in Mg and DIC compared to Na, K, Ca and Cl^-, and are mildly alkaline ($8.5 < pH < 8.9$). As suggested for other serpentinite-hosted (sub-) surface waters, the chemistry of Ronda Mg–HCO_3 river waters is most likely due to hydrolysis of

ferromagnesian peridotite minerals by infiltrated meteoric waters and shallow groundwater that are in equilibrium with the atmosphere. The physicochemical composition of Ronda Ca–OH hyperalkaline fluids is/was derived via low temperature serpentinization reactions from Mg–HCO_3 river waters or Ca–HCO_3 waters from near karst aquifers that infiltrate the peridotites along brittle faults with brecciated serpentinite. Mass balance calculations indicate that weathering of Ca-bearing peridotite is a feasible source of Ca in Ronda Ca–OH hyperalkaline fluids, but it would require relatively high steady-state dissolution rates.

Travertine, crystalline crusts and sediment deposits are the main precipitate types found in the Ronda hyperalkaline spring sites. Calcite and aragonite, minor dolomite and Mg-Al-rich clays are the main minerals in the spring sites. As illustrated in the Baños del Puerto spring (BP) site, (i) calcite-dominated precipitation occurs at atmospheric CO_2-driven uptake of hyperalkaline fluids at their discharging sites, and (ii) aragonite-dominated precipitation occurs by mixing of Ca–OH hyperalkaline fluids with Mg–HCO_3 river waters. Aragonite and dolomite contents increase away from the springs and toward the river waters. The main factors driving the precipitation of different carbonate phases are the Mg concentration, the Mg/Ca ratio, and the carbonic species abundance in the fluids. Textures of calcium carbonates indicate fast supersaturation rates in lithified travertine, and variations in supersaturation rate at calcitic crystalline crusts floating on the surface of the hyperalkaline springs. Variability in aragonite textures reflects fast supersaturation rates as evidenced by crystal branching. Dolomite forms during lithification processes of travertines, and sporadic flooding of river water combined with subsequent evaporation.

Acknowledgements

We thank Francisca Espinosa Pérez and Manuel Jesús Román Alpiste for their help in fieldtrip logistics and technical support, and Cristobal Verdugo Escamilla for assistance with XRD analyses. We acknowledge Dr. Bénédicte Menez and Dr. Marguerite Godard for editorial assistance, and Christophe Monnin and two anonymous reviewers for their thoughtful and very constructive reviews.

The present research has been funded by the European Commission in the framework of the FP7 Marie Curie Action–ITN "ABYSS" under REA grant agreement no. 608001, and European Research Council Advanced Grant "PROMETHEUS" under REA grant agreement no. 340863. CJG acknowledges funding from the Junta de Andalucía (grant nº RNM–131). Research and infrastructure grants leading to this research have been (co)funded by the European Regional Development Fund (ERFD) and the European Social Fund (ESF) of the European Commission.

References

Acosta-Vigil, A., Rubatto, D., Bartoli, O., Cesare, B., Meli, S., Pedrera, A., Azor, A., Tajčmanová, L., 2014. Age of anatexis in the crustal footwall of the Ronda peridotites, S Spain. Lithos 210, 147–167.

Alt, J.C., Garrido, C.J., Shanks III, W.C., Turchyn, A., Padrón-Navarta, J.A., Lopez Sanchez-Vizcaino, V., Gomez Pugnaire, M.T., Marchesi, C., 2012. Recycling of water, carbon, and sulfur during subduction of serpentinites: a stable isotope study of Cerro del Almirez, Spain. Earth Planet. Sci. Lett. 327, 50–60. https://doi.org/10.1016/j.epsl.2012.01.029.

Alt, J.C., Schwarzenbach, E.M., Früh-Green, G.L., Shanks III, W.C., Bernasconi, S.M., Garrido, C.J., Crispini, L., Gaggero, L., Padrón-Navarta, J.A., Marchesi, C., 2013. The role of serpentinites in cycling of carbon and sulfur: seafloor serpentinization and subduction metamorphism. Lithos 178, 40–54.

Andreani, M., Luquot, L., Gouze, P., Godard, M., Hoise, E., Gibert, B., 2009. Experimental study of carbon sequestration reactions controlled by the percolation of CO_2-rich brine through peridotites. Environ. Sci. Technol. 43, 1226–1231.

Argamasilla, M., Barberá, J.A., Andreo, B., 2017. Factors controlling groundwater salinization and hydrogeochemical processes in coastal aquifers from southern Spain. Sci. Total Environ. 580, 50–68.

Arvidson, R.S., Mackenzie, F.T., 1999. The dolomite problem; control of precipitation kinetics by temperature and saturation state. Am. J. Sci. 299, 257–288.

Aquilano, D., Costa, E., Genovese, A., Massaro, F.R., Pastero, L., Rubbo, M., 2003. Hollow rhombohedral calcite crystals encompassing CO_2 microcavities nucleated in solution. J. Cryst. Growth 247, 516–522.

Badiozamani, K., 1973. The dorag dolomitization model, application to the middle Ordovician of Wisconsin. J. Sediment. Res. 43, 965–984.

Ball, J.W., Nordstrom, D.K., 1991. User's manual for WATEQ4F, with revised thermodynamic data base and test cases for calculating speciation of major, trace, and redox elements in natural waters.

Balanyá, J.C., García-Dueñas, V., Azañón, J.M., Sánchez-Gómez, M., 1997. Alternating contractional and extensional events in the alpujarride nappes of the alboran domain (Betics, Gibraltar arc). Tectonics 16, 226–238.

Barberá, J.A., Andreo, B., 2015. Hydrogeological processes in a fluviokarstic area inferred from the analysis of natural hydrogeochemical tracers. The case study of eastern Serranía de Ronda (S Spain). J. Hydrol. 523, 500–514.

Barnes, I., La Marche, V.C., Himmelberg, G., 1967. Geochemical evidence of present-day serpentinization. Science 156, 830–832.

Barnes, I., O'Neil, J.R., 1969. The relationship between fluids in some fresh alpine-type ultramafics and possible modern serpentinization, western United States. Geol. Soc. Am. Bull. 80, 1947–1960.

Barnes, I., O'Neil, J.R., 1971. Calcium-magnesium carbonate solid solutions from Holocene conglomerate cements and travertines in the Coast Range of California. Geochem. Cosmochim. Acta 35, 699–718.

Barnes, I., O'Neil, J.R., Trescases, J.J., 1978. Present day serpentinization in New Caledonia, Oman and Yugoslavia. Geochem. Cosmochim. Acta 42, 144–145.

Baumeister, J.L., Hausrath, E.M., Olsen, A.A., Tschauner, O., Adcock, C.T., Metcalf, R.V., 2015. Biogeochemical weathering of serpentinites: an examination of incipient dissolution affecting serpentine soil formation. Appl. Geochem. 54, 74–84.

Beniash, E., Aizenberg, J., Addadi, L., Weiner, S., 1997. Amorphous calcium carbonate transforms into calcite during sea urchin larval spicule growth. Proc. R. Soc. Lond. B Biol. Sci. 264, 461–465.

Blank, J.G., Green, S.J., Blake, D., Valley, J.W., Kita, N.T., Treiman, A., Dobson, P.F., 2009. An alkaline spring system within the Del Puerto Ophiolite (California, USA): a Mars analog site. Planet. Space Sci. 57, 533–540.

Bodinier, J.L., Garrido, C.J., Chanefo, I., Bruguier, O., Gervilla, F., 2008. Origin of pyroxenite-peridotite veined mantle by refertilization reactions: evidence from the Ronda peridotite (Southern Spain). J. Petrol. 49, 999–1025. https://doi.org/10.1093/petrology/egn014.

Bodinier, J.L., Godard, M., 2006. Orogenic, ophiolitic and abyssal peridotites. In: Carlson, R.W. (Ed.), Treatise on Geochemistry. 2. Geochemistry of the Mantle and Core. Elsevier.

Boetius, A., Ravenschlag, K., Schubert, C.J., Rickert, D., Widdel, F., Gieseke, A., Amann, R., Jorgensen, B.B., Witte, U., Pfannkuche, O., 2000. A marine microbial consortium apparently mediating anaerobic oxidation of methane. Nature 407, 623.

Booth-Rea, G., Martínez-Martínez, J.M., Giaconia, F., 2015. Continental subduction, intracrustal shortening, and coeval upper-crustal extension: P-T evolution of subducted south Iberian paleomargin metapelites (Betics, SE Spain). Tectonophysics 663, 122–139. https://doi.org/10.1016/j.tecto.2015.08.036.

Boschetti, T., Toscani, L., 2008. Springs and streams of the Taro–Ceno Valleys (Northern Apennine, Italy): reaction path modeling of waters interacting with serpentinized ultramafic rocks. Chem. Geol. 257, 76–91.

Bruni, J., Canepa, M., Chiodini, G., Cioni, R., Cipolli, F., Longinelli, A., Marini, L., Ottonello, G., Zuccolini, M.V., 2002. Irreversible water–rock mass transfer accompanying the generation of the neutral, Mg–HCO3 and high-pH, Ca–OH spring waters of the Genova province, Italy. Appl. Geochem. 17, 455–474.

Bundeleva, I.A., Shirokova, L.S., Pokrovsky, O.S., Bénézeth, P., Ménez, B., Gérard, E., Balor, S., 2014. Experimental modeling of calcium carbonate precipitation by cyanobacterium Gloeocapsa sp. Chem. Geol. 374, 44–60.

Burton, E.A., 1993. Controls on marine carbonate cement mineralogy: review and reassessment. Chem. Geol. 105, 163–179.

Cardace, D., Hoehler, T.M., Roberts, B.A., Foster, A.L., 2009. Actively serpentinizing seeps in the Bay of island ophiolites, western newfoundland: a window into the deep biosphere. In: Annual Meeting Geological Society of America Abstracts with Programs, vol. 41, p. 378.

Chavagnac, V., Monnin, C., Ceuleneer, G., Boulart, C., Hoareau, G., 2013a. Characterization of hyperalkaline fluids produced by low-temperature serpentinization of mantle peridotites in the Oman and Ligurian ophiolites. Geochem. Geophys. Geosyst. 14, 2496–2522.

Chavagnac, V., Ceuleneer, G., Monnin, C., Lansac, B., Hoareau, G., Boulart, C., 2013b. Mineralogical assemblages forming at hyperalkaline warm springs hosted on ultramafic rocks: a case study of Oman and Ligurian ophiolites. Geochem. Geophys. Geosyst. 14, 2474–2495.

Cipolli, F., Gambardella, B., Marini, L., Ottonello, G., Zuccolini, M.V., 2004. Geochemistry of high-pH waters from serpentinites of the Gruppo di Voltri (Genova, Italy) and reaction path modeling of CO_2 sequestration in serpentinite aquifers. Appl. Geochem. 19, 787–802.

Dasgupta, R., Hirschmann, M.M., 2010. The deep carbon cycle and melting in Earth's interior. Earth Planet. Sci. Lett. 298, 1–13.

De Boer, J.Z., Chanton, J., Zeitlhöfler, M., 2007. Homer's Chimaera fires (SW of Antalya Turkey); burning abiogenic methane gases; are they generated by a serpentinization process related to alkalic magmatism? Z. Dtsch. Ges. Geowiss. 158, 997–1003.

De Obeso, J.C., Kelemen, P.B., 2018. Fluid rock interactions on residual mantle peridotites overlain by shallow oceanic limestones: insights from Wadi Fins, Sultanate of Oman. Chem. Geol. 498, 139–149. https://doi.org/10.1016/j.chemgeo.2018.09.022.

De Yoreo, J.J., Gilbert, P.U., Sommerdijk, N.A., Penn, R.L., Whitelam, S., Joester, D.,

Zhang, H., Rimer, J.D., Navrotsky, A., Banfield, J.F., Wallace, A.F., Michel, F.M., Meldrum, F.C., Cölfen, H., Dove, P.M., 2015. Crystallization by particle attachment in synthetic, biogenic, and geologic environments. Science 349, aaa6760.
Di Tommaso, D., de Leeuw, N.H., 2010. Structure and dynamics of the hydrated magnesium ion and of the solvated magnesium carbonates: insights from first principles simulations. Phys. Chem. Chem. Phys. 12, 894–901.
Etiope, G., Sherwood Lollar, B., 2013. Abiotic methane on Earth. Rev. Geophys. 51, 276–299.
Etiope, G., Vadillo, I., Whiticar, M.J., Marques, J.M., Carreira, P.M., Tiago, I., Benavente, J., Jiménez, P., Urresti, B., 2016. Abiotic methane seepage in the Ronda peridotite massif, southern Spain. Appl. Geochem. 66, 101–113.
Etiope, G., Whiticar, M.J., 2019. Abiotic methane in continental ultramafic rock systems: towards a genetic model. Appl. Geochem. 102, 139–152. https://doi.org/10.1016/j.apgeochem.2019.01.012.
Faccenna, C., Piromallo, C., Crespo-Blanc, A., Jolivet, L., Rossetti, F., 2004. Lateral slab deformation and the origin of the western Mediterranean arcs. Tectonics 23. https://doi.org/10.1029/2002tc001488.
Falini, G., Gazzano, M., Ripamonti, A., 1994. Crystallization of calcium carbonate in presence of magnesium and polyelectrolytes. J. Cryst. Growth 137, 577–584.
Falk, E.S., Guo, W., Paukert, A.N., Matter, J.M., Mervine, E.M., Kelemen, P.B., 2016. Controls on the stable isotope compositions of travertine from hyperalkaline springs in Oman: insights from clumped isotope measurements. Geochem. Cosmochim. Acta 192, 1–28.
Fernandez-Diaz, L., Putnis, A., Prieto, M., Putnis, C.V., 1996. The role of magnesium in the crystallization of calcite and aragonite in a porous medium. J. Sediment. Res. 66, 482–491.
Fischbeck, R., Müller, G., 1971. Monohydrocalcite, hydromagnesite, nesquehonite, dolomite, aragonite, and calcite in speleothems of the Fränkische Schweiz, Western Germany. Contrib. Mineral. Petrol. 33, 87–92.
Folk, R.L., 1993. SEM imaging of bacteria and nannobacteria in carbonate sediments and rocks. J. Sediment. Res. 63, 990–999.
Folk, R., 1994. Interaction between bacteria, nannobacteria, and mineral precipitation in hot springs of central Italy. Géogr. Phys. Quaternaire 48, 233–246.
Frets, E.C., Tommasi, A., Garrido, C.J., Vauchez, A., Mainprice, D., Targuisti, K., Amri, I., 2014. The Beni Bousera peridotite (Rif belt, Morocco): an oblique-slip low-angle shear zone thinning the subcontinental mantle lithosphere. J. Petrol. 55, 283–313. https://doi.org/10.1093/petrology/egt067.
García-Ruiz, J.M., Hyde, S.T., Carnerup, A.M., Christy, A.G., Van Kranendonk, M.J., Welham, N.J., 2003. Self-assembled silica-carbonate structures and detection of ancient microfossils. Science 302, 1194–1197.
García-Ruiz, J.M., Nakouzi, E., Kotopoulou, E., Tamborrino, L., Steinbock, O., 2017. Biomimetic mineral self-organization from silica-rich spring waters. Sci. Adv. 3, 1602285.
Garrido, C.J., Bodinier, J.L., 1999. Diversity of mafic rocks in the Ronda peridotite: evidence for pervasive melt-rock reaction during heating of subcontinental lithosphere by upwelling asthenosphere. J. Petrol. 40, 729–754.
Garrido, C.J., Gueydan, F., Booth-Rea, G., Précigout, J., Hidas, K., Padron-Navarta, J.A., Marchesi, C., 2011. Garnet lherzolite and garnet-spinel mylonite in the Ronda peridotite: vestiges of Oligocene backarc mantle lithospheric extension in the western Mediterranean. Geology 39, 927–930. https://doi.org/10.1130/G31760.1.
Gervilla, F., Leblanc, M., 1990. Magmatic ores in high-temperature alpine-type lherzolite massifs (Ronda, Spain, and Beni Bousera, Morocco). Econ. Geol. 44, 112–132.
González-Jiménez, J.M., Marchesi, C., Griffin, W.L., Gervilla, F., Belousova, E.A., Garrido, C.J., Romero, R., Talavera, C., Leisen, M., O'Reilly, S.Y., Barra, F., Martin, L., 2017. Zircon recycling and crystallization during formation of chromite- and Ni-arsenide ores in the subcontinental lithospheric mantle (Serranía de Ronda, Spain). Ore Geol. Rev. 90, 193–209. https://doi.org/10.1016/j.oregeorev.2017.02.012.
Grozeva, N.G., 2018. Mineral Transformations in Seafloor Serpentinization Systems. Ph.D. Thesis. MIT, p. 198.
Guerrera, F., Martín-Martín, M., Perrone, V., Tramontana, M., 2005. Tectono-sedimentary evolution of the southern branch of the western tethys (maghrebian flysch basin and lucanian ocean): consequences for western mediterranean geodynamics. Terra. Nova 17, 358–367. https://doi.org/10.1111/j.1365-3121.2005.00621.x.
Hidas, K., Booth-Rea, G., Garrido, C.J., Martínez-Martínez, J.M., Padrón-Navarta, J.A., Konc, Z., Giaconia, F., Frets, E., Marchesi, C., 2013a. Backarc basin inversion and subcontinental mantle emplacement in the crust: kilometre-scale folding and shearing at the base of the proto-Alborán lithospheric mantle (Betic Cordillera, southern Spain). J. Geol. Soc. 170, 47–55.
Hidas, K., Garrido, C.J., Tommasi, A., Padrón-Navarta, J.A., Thielmann, M., Konc, Z., Frets, E., Marchesi, C., 2013b. Strain localization in pyroxenite by reaction-enhanced softening in the shallow subcontinental lithospheric mantle. J. Petrol. 54, 1997–2031.
Hidas, K., Varas-Reus, M.I., Garrido, C.J., Marchesi, C., Acosta-Vigil, A., Padrón-Navarta, J.A., Targuisti, K., Konc, Z., 2015. Hyperextension of continental to oceanic-like lithosphere: the record of late gabbros in the shallow subcontinental lithospheric mantle of the westernmost Mediterranean. Tectonophysics 650, 65–79.
Jones, B., 2017a. Review of calcium carbonate polymorph precipitation in spring systems. Sediment. Geol. 353, 64–75.
Jones, B., 2017b. Review of aragonite and calcite crystal morphogenesis in thermal spring systems. Sediment. Geol. 354, 9–23.
Jones, B., Peng, X., 2016. Mineralogical, crystallographic, and isotopic constraints on the precipitation of aragonite and calcite at Shiqiang and other hot springs in Yunnan Province, China. Sediment. Geol. 345, 103–125.
Kelemen, P.B., Matter, J., 2008. In situ carbonation of peridotite for CO2 storage. Proc. Natl. Acad. Sci. U.S.A. 105, 17295–17300.
Kelemen, P.B., Matter, J., Streit, E.E., Rudge, J.F., Curry, W.B., Blusztajn, J., 2011. Rates and mechanisms of mineral carbonation in peridotite: natural processes and recipes for enhanced, in situ CO_2 capture and storage. Annu. Rev. Earth Planet Sci. 39, 545–576.
Kelemen, P.B., Manning, C.E., 2015. Reevaluating carbon fluxes in subduction zones, what goes down, mostly comes up. Proc. Natl. Acad. Sci. 112, E3997–E4006.
Kelley, D.S., Karson, J.A., Blackman, D.K., FruÈh-Green, G.L., Butterfield, D.A., Lilley, M.D., Olson, E.J., Schrenk, M.O., Roe, K.K., Lebon, G.T., Rivizzigno, P., 2001. An off-axis hydrothermal vent field near the Mid-Atlantic Ridge at 30 N. Nature 412, 145.
Kelley, D.S., Karson, J.A., Früh-Green, G.L., Yoerger, D.R., Shank, T.M., Butterfield, D.A., Hayes, J.M., Schrenk, M.O., Olson, E.J., Proskurowski, G., Jakuba, M., 2005. A serpentinite-hosted ecosystem: the Lost City hydrothermal field. Science 307, 1428–1434.
Kitamura, M., 2001. Crystallization and transformation mechanism of calcium carbonate polymorphs and the effect of magnesium ion. J. Colloid Interface Sci. 236, 318–327.
Klein, F., Garrido, C.J., 2011. Thermodynamic constraints on mineral carbonation of serpentinized peridotite. Lithos 126, 147–160. https://doi.org/10.1016/j.lithos.2011.07.020.
Lacelle, D., Lauriol, B., Clark, I.D., 2009. Formation of seasonal ice bodies and associated cryogenic carbonates in Caverne de l'Ours, Québec, Canada: kinetic isotope effects and pseudo-biogenic crystal structures. J. Cave Karst Stud. 71, 48–62.
Land, L.S., 1998. Failure to precipitate dolomite at 25 ºC from dilute solution despite 1000-fold oversaturation after 32 years. Aquat. Geochem. 4, 361–368.
Leleu, T., Chavagnac, V., Delacour, A., Noiriel, C., Ceuleneer, G., Aretz, M., Rommevaux, C., Ventalon, S., 2016. Travertines associated with hyperalkaline springs: evaluation as a proxy for paleoenvironmental conditions and sequestration of atmospheric CO_2. J. Sediment. Res. 86, 1328–1343.
Lenoir, X., Garrido, C., Bodinier, J., Dautria, J., Gervilla, F., 2001. The recrystallization front of the Ronda peridotite: evidence for melting and thermal erosion of subcontinental lithospheric mantle beneath the Alboran basin. J. Petrol. 42, 141–158. https://doi.org/10.1093/petrology/42.1.141.
Lin, Y.P., Singer, P.C., 2009. Effect of Mg^{2+} on the kinetics of calcite crystal growth. J. Cryst. Growth 312, 136–140.
Lonergan, L., White, N., 1997. Origin of the Betic-Rif mountain belt. Tectonics 16, 504–522.
Lu, G., Zheng, C., Donahoe, R.J., Lyons, W.B., 2000. Controlling processes in a CaCO3 precipitating stream in huanglong natural scenic district, sichuan, China. J. Hydrol. 230, 34–54.
Ludwig, K.A., Kelley, D.S., Butterfield, D.A., Nelson, B.K., Früh-Green, G., 2006. formation and evolution of carbonate chimneys at the Lost city hydrothermal field. Geochem. Cosmochim. Acta 70, 3625–3645.
Marchesi, C., Garrido, C.J., Bosch, D., Bodinier, J.-L., Hidas, K., Padron-Navarta, J.A., Gervilla, F., 2012. A late Oligocene suprasubduction setting in the Westernmost Mediterranean revealed by intrusive pyroxenite dikes in the Ronda Peridotite (Southern Spain). J. Geol. 120, 237–247. https://doi.org/10.1086/663875.
Margiotta, S., Mongelli, G., Summa, V., Paternoster, M., Fiore, S., 2012. Trace element distribution and Cr (VI) speciation in Ca-HCO_3 and Mg-HCO_3 spring waters from the northern sector of the Pollino massif, southern Italy. J. Geochem. Explor. 115, 1–12.
Martín Algarra, A., 1987. Evolucion geologica alpina del contacto entre las zonas internas y las zonas externas de la cordillera Bética (sector centro-occidental). Doctoral dissertation, Universidad de Granada, Spain.
Martin, W., Russell, M.J., 2007. On the origin of biochemistry at an alkaline hydrothermal vent. Philos. Trans. R. Soc. Biol. Sci. 362, 1887–1926.
Martin, W., Baross, J., Kelley, D., Russell, M.J., 2008. Hydrothermal vents and the origin of life. Nat. Rev. Microbiol. 6, 805.
Martinez, R.E., Gardés, E., Pokrovsky, O.S., Schott, J., Oelkers, E.H., 2010. Do photosynthetic bacteria have a protective mechanism against carbonate precipitation at their surfaces? Geochem. Cosmochim. Acta 74, 1329–1337.
Martos-Rosillo, S., González-Ramón, A., Jiménez-Gavilán, P., Andreo, B., Durán, J.J., Mancera, E., 2015. Review on groundwater recharge in carbonate aquifers from SW Mediterranean (Betic Cordillera, S Spain). Environ. Earth Sci. 74, 7571–7581.
Marques, J.M., Carreira, P.M., Carvalho, M.R., Matias, M.J., Goff, F.E., Basto, M.J., Graça, R.C., Aires-Barros, L., Rocha, L., 2008. Origins of high pH mineral waters from ultramafic rocks, Central Portugal. Appl. Geochem. 23, 3278–3289.
Matter, J.M., Kelemen, P.B., 2009. Permanent storage of carbon dioxide in geological reservoirs by mineral carbonation. Nat. Geosci. 2, 837.
Mazzoli, S., Martin Algarra, A., 2011. Deformation partitioning during transpressional emplacement of a 'mantle extrusion wedge': the Ronda peridotites, western Betic Cordillera, Spain. J. Geol. Soc. 168, 373–382. https://doi.org/10.1144/0016-76492010-126.
Mazzoli, S., Martín-Algarra, A., Reddy, S.M., López Sánchez-Vizcaíno, V., Fedele, L., Noviello, A., 2013. The evolution of the footwall to the Ronda subcontinental mantle peridotites: insights from the Nieves Unit (western Betic Cordillera). J. Geol. Soc. 170, 385–402.
McCollom, T.M., Klein, F., Robbins, M., Moskowitz, B., Berquó, T.S., Jöns, N., Bach, W., Templeton, A., 2016. Temperature trends for reaction rates, hydrogen generation, and partitioning of iron during experimental serpentinization of olivine. Geochem. Cosmochim. Acta 181, 175–200. https://doi.org/10.1016/j.gca.2016.03.002.

McCollom, T.M., 2016. Abiotic methane formation during experimental serpentinization of olivine. Proc. Natl. Acad. Sci. https://doi.org/10.1073/pnas.1611843113.
Meldrum, F.C., Cölfen, H., 2008. Controlling mineral morphologies and structures in biological and synthetic systems. Chem. Rev. 108, 4332–4432.
Menzel, M.D., Garrido, C.J., López Sánchez-Vizcaíno, V., Marchesi, C., Hidas, K., Escayola, M.P., Delgado Huertas, A., 2018. Carbonation of mantle peridotite by CO_2-rich fluids: the formation of listvenites in the Advocate ophiolite complex (Newfoundland, Canada). Lithos 323, 238–261. https://doi.org/10.1016/j.lithos.2018.06.001.
Menzel, M.D., Garrido, C.J., Sánchez-Vizcaíno, V.L., Hidas, K., Marchesi, C., 2019. Subduction metamorphism of serpentinite-hosted carbonates beyond antigorite serpentinite dehydration (Nevado-Filábride Complex, Spain). J. Metamorph. Geol. https://doi.org/10.1111/jmg.12481.
Mervine, E.M., Humphris, S.E., Sims, K.W., Kelemen, P.B., Jenkins, W.J., 2014. Carbonation rates of peridotite in the Samail Ophiolite, Sultanate of Oman, constrained through ^{14}C dating and stable isotopes. Geochem. Cosmochim. Acta 126, 371–397.
Monnin, C., Chavagnac, V., Boulart, C., Ménez, B., Gérard, M., Gérard, E., Pisapia, C., Quemeneur, M., Erauso, G., Postec, A., Guentas-Dombrowski, L., 2014. Fluid chemistry of the low temperature hyperalkaline hydrothermal system of Prony Bay (New Caledonia). Biogeosciences 11, 5687–5706.
Morrill, P.L., Kuenen, J.G., Johnson, O.J., Suzuki, S., Rietze, A., Sessions, A.L., Fogel, M.L., Nealson, K.H., 2013. Geochemistry and geobiology of a present-day serpentinization site in California: the Cedars. Geochem. Cosmochim. Acta 109, 222–240.
Müller, D.W., McKenzie, J.A., Mueller, P.A., 1990. Abu Dhabi sabkha, Persian Gulf, revisited: application of strontium isotopes to test an early dolomitization model. Geology 18, 618–621.
Neal, C., Shand, P., 2002. Spring and surface water quality of the Cyprus ophiolites. Hydrol. Earth Syst. Sci. Discuss. 6, 797–817.
Neal, C., Stanger, G., 1983. Hydrogen generation from mantle source rocks in Oman. Earth Planet. Sci. Lett. 66, 315–320.
Neal, C., Stanger, G., 1984. Calcium and magnesium hydroxide precipitation from alkaline groundwaters in Oman, and their significance to the process of serpentinization. Mineral. Mag. 48, 237–241.
Neal, C., Stanger, G., 1985. Past and present serpentinization of ultramafic rocks: An example from the Semail ophiolite nappe of northern Oman. In: Drever, J.I. (Ed.), The Chemistry of Weathering. Springer, pp. 249–275.
Obata, M., Suen, C.J., Dickey, J.S., 1980. The origin of mafic layers in the Ronda high-temperature peridotite intrusion, S. Spain: an evidence of partial fusion and fractional crystallization in the upper mantle. Colloques Internationaux CNRS 272, 257–268.
Orr Chazen, P., Ehrlich, R., 1973. Low-temperature synthesis of dolomite from aragonite. Geol. Soc. Am. Bull. 84, 3627–3634.
Palandri, J.L., Reed, M.H., 2004. Geochemical models of metasomatism in ultramafic systems: serpentinization, rodingitization, and sea floor carbonate chimney precipitation. Geochem. Cosmochim. Acta 68, 1115–1133.
Parkhurst, D.L., Appelo, C.A.J., 2005. PHREEQC-2 Version 2.12: A Hydrochemical Transport Model. US Geological Survey Central Region Research, USGS Water Resources Division. http://wwwbrr.cr.usgs.gov/projects/GWC_coupled/phreeqc.
Paukert, A.N., Matter, J.M., Kelemen, P.B., Shock, E.L., Havig, J.R., 2012. Reaction path modeling of enhanced in situ CO_2 mineralization for carbon sequestration in the peridotite of the Samail Ophiolite, Sultanate of Oman. Chem. Geol. 330, 86–100.
Peckmann, J., Thiel, V., 2004. Carbon cycling at ancient methane–seeps. Chem. Geol. 205, 443–467.
Pentecost, A., 1992. Carbonate chemistry of surface waters in a temperate karst region: the southern Yorkshire Dales, UK. J. Hydrol. 139, 211–232.
Pentecost, A., 2005. Travertine. Springer Science and Business Media.
Platt, J.P., Behr, W.M., Johanesen, K., Williams, J.R., 2013. The betic-rif arc and its orogenic hinterland: a review. Annu. Rev. Earth Planet Sci. 41, 313–357. https://doi.org/10.1146/annurev-earth-050212-123951.
Pope, M.C., Grotzinger, J.P., 2000. Controls on fabric development and morphology of tufas and stromatolites, uppermost Pethel Group (1.8 Ga), Great Slave Lake, northwest Canada. In: Grotzinger, J.P., James, N.P. (Eds.), Carbonate Sedimentation and Diagenesis in the Evolving Precambrian World. SEPM Special Publication, Tulsa, OK.
Précigout, J., Gueydan, F., Garrido, C.J., Cogné, N., Booth-Rea, G., 2013. Deformation and exhumation of the Ronda peridotite (Spain). Tectonics 32, 1011–1025. https://doi.org/10.1002/tect.20062.
Proskurowski, G., Lilley, M.D., Kelley, D.S., Olson, E.J., 2006. Low temperature volatile production at the Lost City Hydrothermal Field, evidence from a hydrogen stable isotope geothermometer. Chem. Geol. 229, 331–343.
Reddy, M.M., Wang, K.K., 1980. Crystallization of calcium carbonate in the presence of metal ions: I. Inhibition by magnesium ion at pH 8.8 and 25°C. J. Cryst. Growth 50, 470–480.
Rempfert, K.R., Miller, H.M., Bompard, N., Nothaft, D., Matter, J.M., Kelemen, P., Fierer, N., Templeton, A.S., 2017. Geological and geochemical controls on subsurface microbial life in the Samail Ophiolite, Oman. Front. Microbiol. 8, 56.
Renaut, R.W., Jones, B., 1997. Controls on aragonite and calcite precipitation in hot spring travertines at Chemurkeu, Lake Bogoria, Kenya. Can. J. Earth Sci. 34, 801–818.
Rietveld, H., 1969. A profile refinement method for nuclear and magnetic structures. J. Appl. Crystallogr. 2, 65–71.
Roberts, J.A., Bennett, P.C., González, L.A., Macpherson, G.L., Milliken, K.L., 2004. Microbial precipitation of dolomite in methanogenic groundwater. Geology 32, 277–280.
Roberts, J.A., Kenward, P.A., Fowle, D.A., Goldstein, R.H., González, L.A., Moore, D.S., 2013. Surface chemistry allows for abiotic precipitation of dolomite at low temperature. Proc. Natl. Acad. Sci. 110, 14540–14545.
Rogerson, M., Pedley, H.M., Kelham, A., Wadhawan, J.D., 2014. Linking mineralisation process and sedimentary product in terrestrial carbonates using a solution thermodynamic approach. Earth Surf. Dyn. 2, 197.
Royden, L.H., 1993. Evolution of retreating subduction boundaries formed during continental collision. Tectonics 12, 629–638.
Sánchez-Murillo, R., Gazel, E., Schwarzenbach, E.M., Crespo-Medina, M., Schrenk, M.O., Boll, J., Gill, B.C., 2014. Geochemical evidence for active tropical serpentinization in the Santa Elena Ophiolite, Costa Rica: an analog of a humid early Earth? Geochem. Geophys. Geosyst. 15, 1783–1800.
Sánchez-Román, M., McKenzie, J.A., Wagener, A.D.L.R., Riva de Neyra, M.A., Vasconcelos, C., 2009. Presence of sulfate does not inhibit low-temperature dolomite precipitation. Earth Planet. Sci. Lett. 285, 131–139.
Sleep, N.H., Bird, D.K., Pope, E.C., 2011. Serpentinite and the dawn of life. Philos. Trans. R. Soc. Biol. Sci. 366, 2857–2869.
Soustelle, V., Tommasi, A., Bodinier, J.L., Garrido, C.J., Vauchez, A., 2009. Deformation and reactive melt transport in the mantle lithosphere above a large-scale partial melting domain: the Ronda Peridotite massif, Southern Spain. J. Petrol. 50, 1235–1266. https://doi.org/10.1093/petrology/egp032.
Stanger, G., 1987. The Hydrogeology of the Oman Mountains. Ph.D. thesis, Department of Earth Sciences, The Open University, U.K.
Stumm, W., Morgan, J.J., 1996. Aquatic Chemistry: Chemical Equilibria and Rates in Natural Waters, third ed. John Wiley and Sons.
Suarez, D.L., 1983. Calcite supersaturation and precipitation kinetics in the lower Colorado river, all-American canal and east highline canal. Water Resour. Res. 19, 653–661.
Taylor, P.M., Chafetz, H.S., 2004. Floating rafts of calcite crystals in cave pools, central Texas, USA: crystal habit vs. saturation state. J. Sediment. Res. 74, 328–341.
Tubía, J.M., 1994. The Ronda peridotites (Los Reales nappe) - an example of the relationship between lithospheric thickening by oblique tectoniques and late extensional deformation within the Betic Cordillera (Spain). Tectonophysics 238, 381–398.
Tubía, J.M., Cuevas, J., Esteban, J.J., 2004. Tectonic evidence in the Ronda peridotites, Spain, for mantle diapirism related to delamination. Geology 32, 941–944.
Tubía, J.M., Cuevas, J., Ibarguchi, J.G., 1997. Sequential development of the metamorphic aureole beneath the Ronda peridotites and its bearing on the tectonic evolution of the Betic Cordillera. Tectonophysics 279, 227–252.
Vadillo, I., Urresti, B., Jiménez, P., Martos, S., José Durán, J., Benavente, J., Carrasco, F., Pedrera, A., 2016. Preliminary hydrochemical study of Ronda ultramafic massif (South Spain). In: European Geosciences Union General Assembly, Conference Abstracts, vol. 18, p. 13275.
Van der Wal, D., Vissers, R.L., 1996. Structural petrology of the Ronda peridotite, SW Spain: deformation history. J. Petrol. 37, 23–43.
Van Lith, Y., Warthmann, R., Vasconcelos, C., McKenzie, J.A., 2003. Microbial fossilization in carbonate sediments: a result of the bacterial surface involvement in dolomite precipitation. Sedimentology 50, 237–245.
Varas-Reus, M.I., Garrido, C.J., Marchesi, C., Bosch, D., Hidas, K., 2018. Genesis of ultra-high pressure garnet pyroxenites in orogenic peridotites and its bearing on the compositional heterogeneity of the Earth's mantle. Geochem. Cosmochim. Acta 232, 303–328.
Vasconcelos, C., McKenzie, J.A., Bernasconi, S., Grujic, D., Tiens, A.J., 1995. Microbial mediation as a possible mechanism for natural dolomite formation at low temperatures. Nature 377, 220.
Vasconcelos, C., McKenzie, J.A., 1997. Microbial mediation of modern dolomite precipitation and diagenesis under anoxic conditions (Lagoa Vermelha, Rio de Janeiro, Brazil). J. Sediment. Res. 67, 378–390.
Vauchez, A., Garrido, C.J., 2001. Seismic properties of an asthenospherized lithospheric mantle: constraints from lattice preferred orientations in peridotite from the Ronda massif. Earth Planet. Sci. Lett. 192, 235–249.
Warthmann, R., Vasconcelos, C., Sass, H., McKenzie, J.A., 2005. Desulfovibrio brasiliensis sp. nov., a moderate halophilic sulfate-reducing bacterium from Lagoa Vermelha (Brazil) mediating dolomite formation. Extremophiles 9, 255–261.
Zeller, E.J., Wray, J.L., 1956. Factors influencing precipitation of calcium carbonate. AAPG (Am. Assoc. Pet. Geol.) Bull. 40, 140–152.
Zhang, F., Xu, H., Konishi, H., Kemp, J.M., Roden, E.E., Shen, Z., 2012. Dissolved sulfide-catalyzed precipitation of disordered dolomite: implications for the formation mechanism of sedimentary dolomite. Geochem. Cosmochim. Acta 97, 148–165.
Zhang, R., Zhang, X., Guy, B., Hu, S., De Ligny, D., Moutte, J., 2013. Experimental study of dissolution rates of hedenbergitic clinopyroxene at high temperatures: dissolution in water from 25 °C to 374 °C. Eur. J. Mineral. 25, 353–372. https://doi.org/10.1127/0935-1221/2013/0025-2268.